Korean J. Chem. Eng., 38(2), 227-247 (2021)
DOI: 10.1007/s11814-020-0693-0
pISSN: 0256-1115
eISSN: 1975-7220

INVITED REVIEW PAPER

Recent advances in the synthesis of mesoporous materials and their application to lithium-ion batteries and hybrid supercapacitors

Eunho Lim*,‡, Jinyoung Chun,‡, Changshin Jo***,†, and Jongkook Hwang****,†**

*Chemical & Process Technology Division, Korea Research Institute of Chemical Technology (KRICT), 141 Gajeongro, Daejeon 34114, Korea
**Energy & Environment Division, Korea Institute of Ceramic Engineering and Technology (KICET), Jinju, Gyeongnam 52851, Korea
***School of Chemical Engineering & Materials Science, Chung-Ang University (CAU), 84 Heukseok-ro, Dongjak-gu, Seoul 06974, Korea
****Department of Chemical Engineering, Ajou University, Worldcupro 206, Suwon 16499, Korea
(*Received 25 August 2020 • Revised 22 September 2020 • Accepted 3 October 2020*)

Abstract−The ever-growing demand for high performance energy storage systems has fueled the development of advanced electrode materials with light weight, high energy/power densities, and stable cycle life. Mesoporous materials play an important role in achieving these goals because of their unique features such as high surface area, tunable pore size, pore volume, and pore structures, as well as adjustable particle size and morphology. In this review, we summarize the recent progress in the synthesis of mesoporous materials and their applications in lithium-ion batteries (LIBs) and lithium-ion hybrid supercapacitors (Li-HSCs) over the past ten years. The block copolymer guided soft-template route is highlighted as a simple and versatile tool for designing mesoporous materials with controlled nano- and macrostructures without complicated synthetic procedures. The structural/morphological benefits of designed mesoporous materials translate into highly improved electrochemical performance in LIBs and Li-HSCs. Finally, future challenges and perspectives on the development of mesoporous materials in energy storage devices are provided, which will be useful both in academia and in industry.

Keywords: Mesoporous Materials, Soft Templating Route, Lithium-ion Batteries, Lithium-ion Hybrid Supercapacitors

INTRODUCTION

Rapidly increasing worldwide energy consumption and heavy dependence on fossil fuels has prompted the utilization of clean, renewable energy sources [1-3]. Advanced energy storage technologies are essential for efficient utilization of renewable energies (*e.g.*, solar and wind energy) which are unstable in output power and uneven in energy distribution [1,4,5]. In addition, the demand for energy storage devices suitable for real world applications such as portable electronics and electric vehicles is rapidly increasing [6-8]. Thus, for the past decade, considerable research effort has been devoted to development of high performance energy storage devices (*e.g.*, lithium-ion batteries (LIBs), supercapacitors, lithium-sulfur batteries) with high energy/power density and long-term stability. One of the most extensively investigated strategies to achieve such goal is the use of nanostructured materials as high capacity electrodes [9-11]. A wide range of nanomaterials with different sizes, morphologies and dimensions have been reported [9, 10]. Among the various candidates, mesoporous materials with pore sizes in the range of 2-50 nm have been of particular research interest because of their multi-capability to absorb, store and interact with guest species in the pore space and surfaces [12-18]. (i) As the electrochemical reactions are surface or electrode-electrolyte interface related process, high surface area can provide a large number of reaction sites for energy storage. (ii) The adjustable pore size and structures are highly useful for increasing mass transport capability (*e.g.*, facile electrolyte transportation) which is important to achieve high capacity retention, especially at high C-rates. In addition, they increase the accessibility of active sites and thus enable full-utilization of electrode materials with minimum dead surface area. For example, introduction of large mesopores and/or macropores (>50 nm) into microporous (<2 nm) materials greatly increases the effective electrochemical surface area and the number of accessible active sites, which are advantageous to preparing high capacity electrode materials. (iii) Large pore volume effectively alleviates the mechanical strain of electrodes caused by volume change during repeated charging/discharging cycles. Furthermore, large pore volume enables high loading of additional guest species with high capacity or catalytic effects [19]. (iv) Mesoporous structures can provide unique nanoscale effects [14]. Mesostructured walls are typically as thin as 10 nm and consist of nanocrystals, and these features can greatly promote solid-state Li^+ diffusion, the rate-limiting step of LIB, thereby increasing rate performance of the electrodes.

In this review, we focus on recent progress in synthesis and application of mesoporous materials as advanced electrode materials in

†To whom correspondence should be addressed.
E-mail: changshin@cau.ac.kr, jongkook@ajou.ac.kr
‡These authors contributed equally.

LIBs and lithium-ion hybrid supercapacitors (Li-HSC) over the last ten years. We summarize the synthesis methods of mesoporous materials with particular emphasis on simultaneous nano- and macro-structure control *via* soft templating routes. Next, we highlight the key literature in the use of mesoporous materials as electrodes in LIBs and Li-HSCs. The structural benefits of mesoporous materials and underlying storage mechanism for each device are described. Finally, we provide future challenges and our perspective on the development of mesoporous materials in energy storage devices.

SYNTHESIS STRATEGIES

1. Soft Templating Route

The synthesis strategies can be categorized into three groups: template-free, hard templating and soft templating method. The template-free method has attracted great attention as an inexpensive and simple route for preparing mesoporous materials potentially suitable for industrial mass production. Template-free approach usually relies on bottom-up aggregation of molecular or nanoscale building blocks [20]. A representative example of such is reticular chemistry-based synthesis of metal-organic frameworks (MOFs), which are constructed by coordination of inorganic metal nodes and organic linkers [21]. MOFs typically have crystalline micropores, but in some cases the pores can be expanded to mesopore range [22]. However, template-free routes generally lack the ability to control the mesopore sizes and structures considerably, and often only produce disordered random mesopores [23-27]. Hard templating route (*i.e.*, nanocasting) employs pre-synthesized "hard" scaffolds such as silica, carbon and colloidal crystals as sacrificial templates. The hard templates act as rigid supports that keep the mesoporous structures intact during heat treatment at high temperature >500 °C, allowing preparation of highly crystalline ordered mesoporous materials. However, this route usually requires time-consuming multistep procedures such as preparation of hard templates, repetitive infiltration of precursors and heat treatments, and template removal. Furthermore, the pore structure and particle morphology are limited and difficult to control because they are inverse replicas of the parent hard templates. Soft templating uses "soft" organic amphiphiles such as surfactant and block copolymer (BCP) as templates. The soft template and diverse organic/inorganic building block (polymer, metal nanoparticles, inorganic sol, etc.) co-assemble to form organic-inorganic hybrid composites through direct precipitation or evaporation induced self-assembly (EISA). Subsequent removal of soft template *via* solvent extraction and/or pyrolysis yields ordered mesoporous materials.

In particular, the soft templating route has been subject of intensive research because it is simple and versatile yet provides considerable controllability and flexibility in the synthesis of mesoporous materials. This can be achieved by controlling the properties of soft template (molar mass, molecular architecture, volume ratio of hydrophobic/hydrophilic block) and guest building blocks (size, surface functionalities, chemical compositions). In 1992, the first soft templating route for ordered mesostructures (~2 nm pores) was reported by Mobil researchers using cationic molecular surfactant [28]. Early research focused on controlling the textural properties of mesoporous materials, such as pore size, structures and wall thickness. Along this line, instead of low-molar-mass surfactants, Stucky and coworkers used commercial pluronic P123 as a soft template to prepare ordered mesoporous silica with pore sizes from 5 to 30 nm [29]. Wiesner and coworkers used lab-made poly(isoprene)-*block*-poly(ethylene oxide) (PI-*b*-PEO) with different molar masses to synthesize mesoporous aluminosilicates with adjustable pore sizes of 10-50 nm [30]. In 1998, the Stucky group further extended the use of P123 for synthesis of diverse mesoporous metal oxides and mixed oxides through EISA [31]. However, pluronic BCPs consist of thermally unstable PEO and poly(propylene oxide) and thus easily decompose under relatively low temperature <400 °C, which is insufficient for full conversion of amorphous state to crystalline state. Therefore, the obtained materials are usually semi-crystalline and go through structural collapse upon heat treatment at elevated temperature. To circumvent this problem, Lee et al. provided a simple and straightforward approach referred to as CASH (combined assembly by soft and hard chemistries) in 2008 [32]. Instead of direct calcination under air, they introduced an intermediate carbonization step at elevated temperature as high as 1,000 °C. During this process, the sp^2-hybridized-carbon-containing PI block of PI-*b*-PEO templates is converted to amorphous carbons which act as rigid hard scaffolds that keep the mesostructured intact during high temperature crystallization. Inspired by this, researchers have used various sp^2-hybridized carbon containing amphiphilic block copolymers such as poly(ethylene oxide)-*b*-poly(styrene) (PEO-*b*-PS), poly(styrene)-*b*-poly(2-vinylpyridine)-*b*-poly(ethylene oxide) (PS-*b*-P2VP-*b*-PEO), poly(styrene)-*b*-poly(2-vinylpyridine) (PS-*b*-P2VP) as advanced soft templates [33]. Among these lab-made polymers, PEO-*b*-PS has been a choice of researchers because of its easy synthesis, strong hydrophilic/hydrophobic contrast between PEO and PS, and high glass transition temperature of PS block. Over the past decade, significant progress has been made in development of ordered mesoporous materials using PEO-*b*-PS as a versatile soft template and structure directing agent.

2. Block Copolymer Guided Co-assembly for Mesoporous Materials

The key requirement for controlled mesostructure formation is selective mixing of guest precursors either into the hydrophilic PEO or the hydrophobic PS without phase segregation. To achieve this, tailoring the enthalpic and entropic interactions between the precursors and PEO-*b*-PS is necessary [34]. The co-assembly should be driven by enthalpically favorable interactions such as hydrogen bonding and electrostatic interaction. The enthalpic interactions are mainly tailored by the surface chemistry of guest building blocks (*e.g.*, functionalization and ligand stabilization). On the other hand, the entropic change upon mixing is mostly governed by the relative size of PEO block to the guest building blocks. For favorable entropic changes upon mixing (*i.e.*, for increasing overall system entropy upon mixing), the guest nanoparticles (NPs) should be smaller than the PEO block which they mix. When the diameter (d) of NP is smaller than the radius of gyration (R_g) of the compatible PEO block ($d<R_g$), the NPs can be mixed within the PEO microdomain uniformly, and thus they co-assemble to form mesostructures. However, when NPs are larger than R_g of the PEO block ($d>R_g$), the NPs tend to segregate out from PEO-microdomain due

to the loss of conformational entropy, thereby leading to complete macrophase separation between NP phase and PEO-*b*-PS phase. This principle is valid for the other guest building blocks such as homopolymers, inorganic sol, and hydrophobic metal precursors.

On the basis of these considerations, a wide range of ordered mesoporous materials with different structures and compositions have been prepared. Most inorganic precursors (transition metal precursors) are highly reactive toward hydrolysis and condensation, imposing great limitation on preparing inorganic building blocks suitable for controlled co-assembly with PEO-*b*-PS (*e.g.*, the hydrolysis of titanium alkoxide is around 10^5 time faster than silicon alkoxide). Thus, non-hydrolytic sol-gel chemistry, acid-base pair chemistry, and various charge- and electrostatic interaction chemistry (*e.g.*, S^+I^-, S^-I^+, $S^+X^-I^+$, S^0I^0, $S^0H^+X^-I^+$ interactions where S=surfactant, I=inorganic moieties, and X=mediating ion) have been proposed [37,38]. For example, combination of non-hydrolytic sol-gel reaction between niobium chloride and niobium alkoxide and CASH strategy enabled formation highly ordered mesoporous Nb_2O_5 with excellent thermal stability and high crystallinity [39,40]. The addition of a small amount of strong acid (HCl, HNO_3) in non-aqueous volatile solvent (tetrahydrofuran (THF)) also effectively produces small inorganic sol (nanoparticles) with plenty of surface hydroxyl groups, which leads to controllable co-assembly and mesostructure formation [41-43]. However, many common metal oxide precursors do not have sufficiently strong enthalpic interactions with soft templates. In addition, mesoporous metal oxides with low

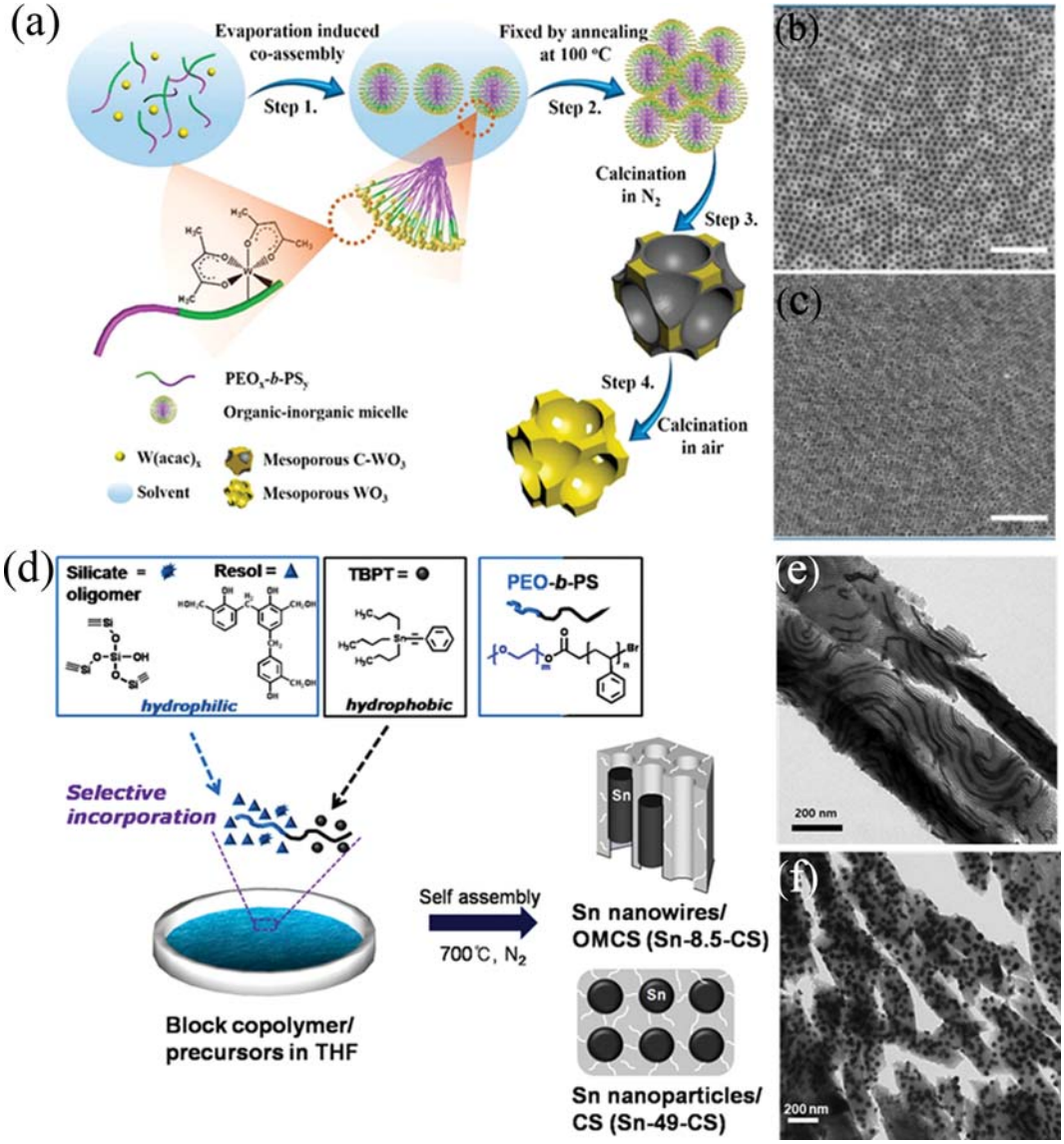

Fig. 1. (a) Schematic illustration of the formation of ordered mesoporous WO_3 *via* acetylacetone (AcAc)-assisted evaporation induced self-assembly, and (b), (c) representative scanning electron microscopy (SEM) images of WO_3 with different mesopore sizes (Reprinted with permission from Ref. [35], Copyright 2017 American Chemical Society), (d) Schematic representation of the synthesis of Sn/carbon-silica composites (Sn-CS), transmission electron microscopy (TEM) images of (e) ordered mesostructures with Sn nanowires confined in nanochannels and (f) Sn nanoparticles confined in nanoporous CS frameworks (Reprinted with permission from Ref. [36], Copyright 2013 American Chemical Society).

crystallization temperature such as ZnO and Co_3O_4 are difficult to synthesize through conventional direct co-assembly method. To strengthen the interaction between precursors and soft template, various ligand-assisted and resol-assisted strategies were developed. Zhao and coworkers reported the use of the coordination agent acetylacetone (AcAc) to slow the hydrolysis and condensation of titanium isopropoxide and increase its interaction with the PEO segment through stronger hydrogen bonding [44]. AcAc-assisted strategy was extended to other kinds of metal oxides including WO_3 and SnO_2. The addition of AcAc to the co-assembly of WCl_6 with PEO-*b*-PS allowed for a more reproducible and reliable WO_3 synthesis compared with the synthesis without AcAc (Fig. 1(a)-(c)) [35]. In a similar manner, ordered mesoporous SnO_2 was obtained by using HCl-AcAc dual-ligand assisted co-assembly [45]. In addition, citric acid, a more powerful tridentate chelating agent with three carboxyl groups, stabilized Zn salts and enhanced their interaction with PEO-*b*-PS, enabling the synthesis of ordered mesoporous ZnO [46]. Resol is oligomeric phenol-formaldehyde resin that has been widely used as an organic precursor to prepare ordered mesoporous carbon. Its abundant hydroxyl and methylol groups simultaneously interact with hydrophilic PEO segments *via* hydrogen bonding and metal ions *via* coordination bonding. Thus, resol can act as a glue and bridge that brings the metal species to block copolymer together, and already has shown promise in preparation of various mesoporous transition metal oxide and their carbon composites (Sn/C, Ge/GeO_2/C, WO_3/C, CoO_x/C) [36,43,47-49]. Recently, Kim et al. utilized a melamine-formaldehyde (MF) resin as an interaction mediator to prepare highly porous MoO_2/C and MoC/C composites [50]. MF resin can well-mix and cross-link with resol, and its nitrogen-functionality has a strong affinity for phosphomolybdic acid (Mo precursor). As a result, MF resin stabilizes Mo precursors and drags them into hydrophilic PEO block forcibly. In a control experiment without MF resin, only large and highly aggregated Mo species were obtained. This observation further demonstrates the role of MF resins as efficient interaction mediators for controlled co-assembly.

As mentioned, the synthesis method of mesoporous materials has been relatively well-established; however, controlling the spatial location of guest species in the mesoporous materials still remains largely unexplored. In particular, selective incorporation of metal nanoparticles (*e.g.*, high capacity electrode materials, catalytic active sites) either in the pores or in the walls has been a challenging task. Pre-synthesized nanocrystals were the first choice of guest species for BCP-directed co-assembly, as methods to control nanocrystal size and tune the functionalities of surface ligands are already known in previous literature [34,51]. However, surface ligands are usually bulky and occupy a significant portion of pre-synthesized nanocrystals, limiting their solubility in BCP microdomains and causing complete macrophase segregation from mesostructures. In addition, surface ligands should be removed to expose the active sites of metal nanoparticles, and this process requires time-consuming ligand stripping or additional heat treatment that can lead to undesired nanocrystal sintering and aggregation [52]. Therefore, the development of a simple method that simultaneously directs the spatial location of guest nanoparticles as well as the formation of ordered mesoporous support is highly desired. In this regard, Lee and coworkers developed one-pot synthesis of metal nanoparticles/mesoporous support composite materials. The method uses the selective interaction among the precursors and block copolymer, PEO-*b*-PS; hydrophilic precursors are selectively mixed with PEO block, whereas hydrophobic metal precursors are incorporated to PS block exclusively. After the co-assembly, the as-made hybrid materials are heat-treated at the desired temperature and gas atmosphere. Hence, metal nanoparticles supported in the pores of mesoporous materials are easily synthesized by simply adding suitable hydrophobic metal precursor into the synthesis conditions for conventional mesoporous materials. In this way, various combinations of metal NPs supported on mesoporous materials are prepared, including Pt/Nb_2O_5 [53], FePt/aluminosilicate [54], Ru/aluminosilicate [55], PtPb/carbon-silica (CS) [56] and Pt_3Co/CS [57]. Interestingly, the Lee group found unique phase behavior in the one-pot assembly of hydrophobic Sn precursor, hydrophilic resol and silicate precursor, and PEO-*b*-PS (Fig. 1(d)) [36]. Hydrophilic resol and silicates mixed with PEO block and hydrophobic Sn precursor selectively incorporated to PS block. When the loading of Sn precursor was low<10 wt%, Sn precursors were well-confined within the PS microdomains and converted to Sn nanowires in the nanochannel of ordered mesoporous CS frameworks (Fig. 1(e)). Due to the low melting point of Sn metal, carbothermally reduced Sn metal droplets are aggregated to form Sn nanowires. When the loading of Sn precursor increased to 49 wt%, a complete phase transition from Sn nanowires to Sn nanoparticles occurred to stabilize the hydrophobic Sn precursor with a fixed amount of PEO-*b*-PS and reduce the overall surface-to-volume ratio. As a result, uniform sized Sn nanoparticles were embedded in CS matrix (Fig. 1(f)). The resulting Sn/CS nanostructured materials were used as anode materials in LIB and showed high specific capacity (600 mAh g^{-1}) and good cycle stability with high Coulombic efficiency. So far, several commercial hydrophobic metal precursors (Pt, Pb, Fe, Ru, Co, and Sn) have been found to be useful in this one-pot co-assembly, such as (dimethyl-(1,5-cyclooctadiene) platinum(II)), (triphenyl(phenylethynyl)lead), (dimethyl aminomethyl ferrocene), bis(2-methylallyl)(1,5-cyclooctadiene)ruthenium(II), cobalt(II) phthalocyanine and tributylphenyltin.

3. Block Copolymer Guided Macrostructure Control of Mesoporous Materials

There has been a growing demand for new approaches to control macrostructures (particle morphologies and macropores) of mesoporous materials without complicated multi-step procedures. In amphiphilic BCPs, the immiscible hydrophilic block and hydrophobic block are linked through covalent bonds, which leads to spontaneous microphase separation in a size regime of 5-100 nm. Therefore, to control macrostructures larger than 100 nm, additional macroscale templates such as foam and colloidal crystals further need to be combined with BCPs. Most of previous literature focused on the use of multiple templates with different length scales through step-by-step approaches which are tedious and laborious. In addition, they considerably lack controllability and flexibility in adjusting pore size, pore structure and particle shape. Therefore, the development of a simple and versatile synthesis method for macrostructure-controlled mesoporous materials has been of particular importance in porous materials society.

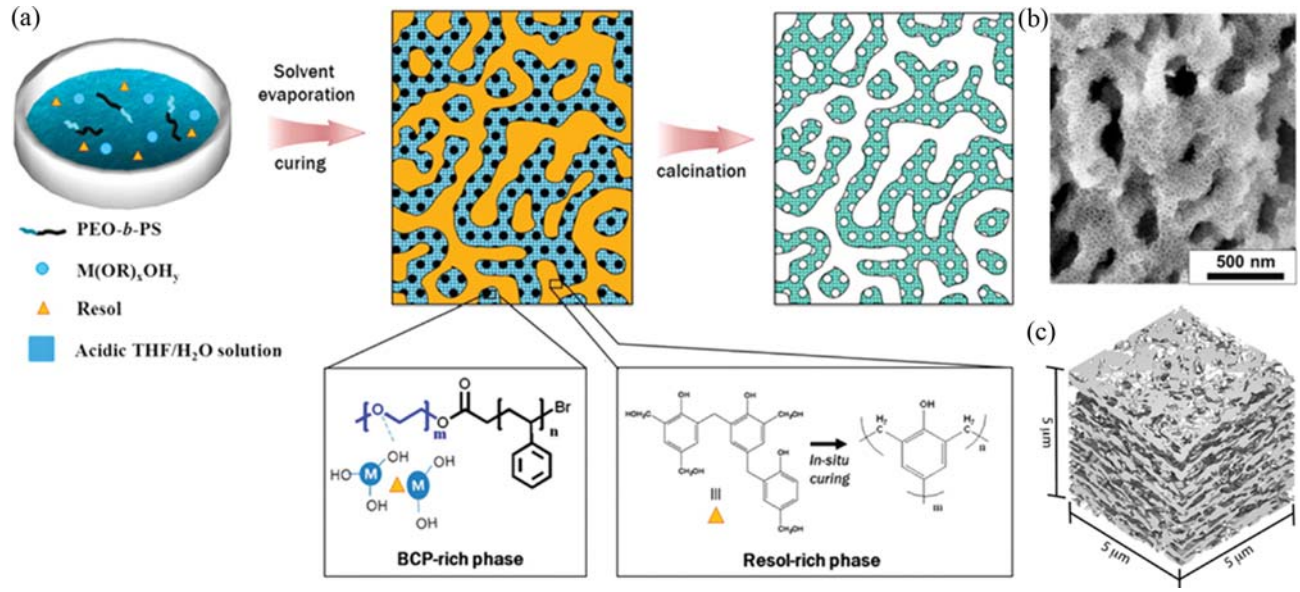

Fig. 2. (a) Schematic illustration of combined hierarchical assembly of micro- and macrophase separation (CHAMPS), (b) SEM image of hierarchically porous silica, and (c) visualization of 3D macrostructures *via* nanoscale computed tomography reconstruction (Reprinted with permission from Ref. [42], Copyright 2014 American Chemical Society).

During BCP-directed multicomponent co-assembly, macroscale phase separation frequently occurs because of solubility limits and weak interaction between precursors and BCPs. Previously, macrophase separation (>100 nm) itself was considered as undesirable phase behavior that should be suppressed/inhibited for formation of ordered mesoporous structures. However, if macrophase separation can be predicted and tamed in a controlled manner, it would become a useful tool to control macrostructures of mesoporous materials. Spinodal decomposition is a representative macrophase separation mechanism that has been intensively studied in materials chemistry (ceramics, alloys) and polymer physics (polymer blends) [58-61]. In a supersaturated mixture, spinodal decomposition can be induced by infinitesimal fluctuation such as rapid temperature change, chemical reaction and solvent removal. Of particular interest are hierarchically porous materials which combine the advantages of macropores (large pore volume and fast mass transport), meso- and micropores (high surface area and accessible active sites). In 2014, Hwang et al. reported combined hierarchical assembly of micro- and macrophase separation (CHAMPS) method for direct synthesis of hierarchically macro-mesoporous inorganic oxide materials (SiO_2 and TiO_2) (Fig. 2(a)) [42]. They simply added concentrated HCl to the mixture of resol, inorganic sol, PEO-*b*-PS dissolved in THF. During solvent evaporation, THF evaporated first and the relative concentration of acid in the solution increased accordingly. This strong acidic environment triggered acid-catalyzed *in-situ* polymerization of resol during self-assembly. In the meantime, PEO-*b*-PS and inorganic precursor (silica and titania sol) co-assembled to form ordered mesoporous structures. Polymerizing resol was expelled from BCP-rich mesostructures and produced independent resol-rich organic domains. Calcination at 550 °C under air removed all organic compounds and generated macropores from resol-rich phase and mesopores from PEO-*b*-PS (Fig. 2(b)). Both pore systems created three dimensionally interconnected pore networks, which were visualized and quantitatively analyzed by nanoscale computed tomography (NanoCT) (Fig. 2(c)). As a consequence, hierarchically porous inorganic oxides having simultaneously adjustable mesopores (15-50 nm) and macropores 50-400 nm) were prepared. The benefits of unique pore systems were confirmed by using the resulting TiO_2 as anode material in LIB, which showed highly enhanced rate capability and capacity retention at high C-rates. On the other hand, *in-situ* polymerized resol can be also used as chelating agent that directs the macrophase separation of inorganic precursors. Kim et al. utilized the chelating ability of resol to directly produce functional macrodomain-integrated mesoporous Nb_2O_5 [62]. Resol can form resol-Nb complexes by chelating. Part of resol-Nb interacted with PEO block of BCPs *via* hydrogen bonding, while the *in-situ* polymerized resol-Nb complexes segregated from BCP-domains to form independent resol-Nb macrodomains. After calcination, ordered mesoporous Nb_2O_5 with submicrometer-sized Nb_2O_5 particles embedded therein was obtained. When applied as a working electrode in dye-sensitized solar cells, the hierarchical Nb_2O_5 increased power conversion efficiency because of the combined function of submicron-sized particles (light scattering) and mesostructures (high dye loading). Jo et al. proposed a new synthesis system that induces macrophase separation by rapidly evaporating volatile solvent from a multicomponent mixture [63]. A homogeneous mixture of PEO-*b*-PS/Nb and Ti precursor/HNO_3 underwent dual phase separation during EISA. Volatile THF evaporates rapidly and preferentially, acting as a stimulus for macrophase separation between (precursors/BCP)-rich phase and HNO_3-rich phase. Since the rate of HNO_3 evaporation is much slower than that of THF, the HNO_3-rich phase evaporated after the onset of macrophase separation. Subsequent evaporation of HNO_3 left empty voids such as isolated macropores or continuous macropores. By controlling the relative amount of HNO_3 and the rate of solvent evaporation, various transition

metal oxide mesoporous materials (TiO_2, $TiNb_2O_7$, WO_3) with isolated macropores, continuous macropores and spherical particle shape were prepared. Interestingly, the use of silicate and resol under the similar synthesis condition enabled synthesis of large pore (29 nm) mesoporous silica nanoparticles (~150 nm) [64]. Macrophase separation between silicate/HNO_3 and polymerizing resol occurred during fast THF evaporation. In the confined space of HNO_3-rich domains, the shape of co-assembled (silicate/PEO-*b*-PS)-phase evolved to isotropic spheres to minimize the total interfacial energy.

Controlling the macroscopic particle morphology (*e.g.*, uniform and regular geometry such as spheres, bowls, sheet and hierarchical architectures) is of high importance to maximize the potential use of mesoporous materials in a wide range of applications in energy devices. For example, uniform particle morphology facilitates the formation of densely packed electrode materials which are advantageous for the development of energy devices with high volumetric capacity [23,27,66]. Lee and coworkers designed a novel approach for generalized synthesis of inorganic mesoporous particles *via* employing the unique phase behaviour of multicomponent polymer blends (Fig. 3(a), (b)) [65]. They provided design criteria for controllable integration of mesoscale BCP microphase separation and macroscale spinodal decomposition to control materials' nano- and macrostructures, respectively. The use of hydropho-

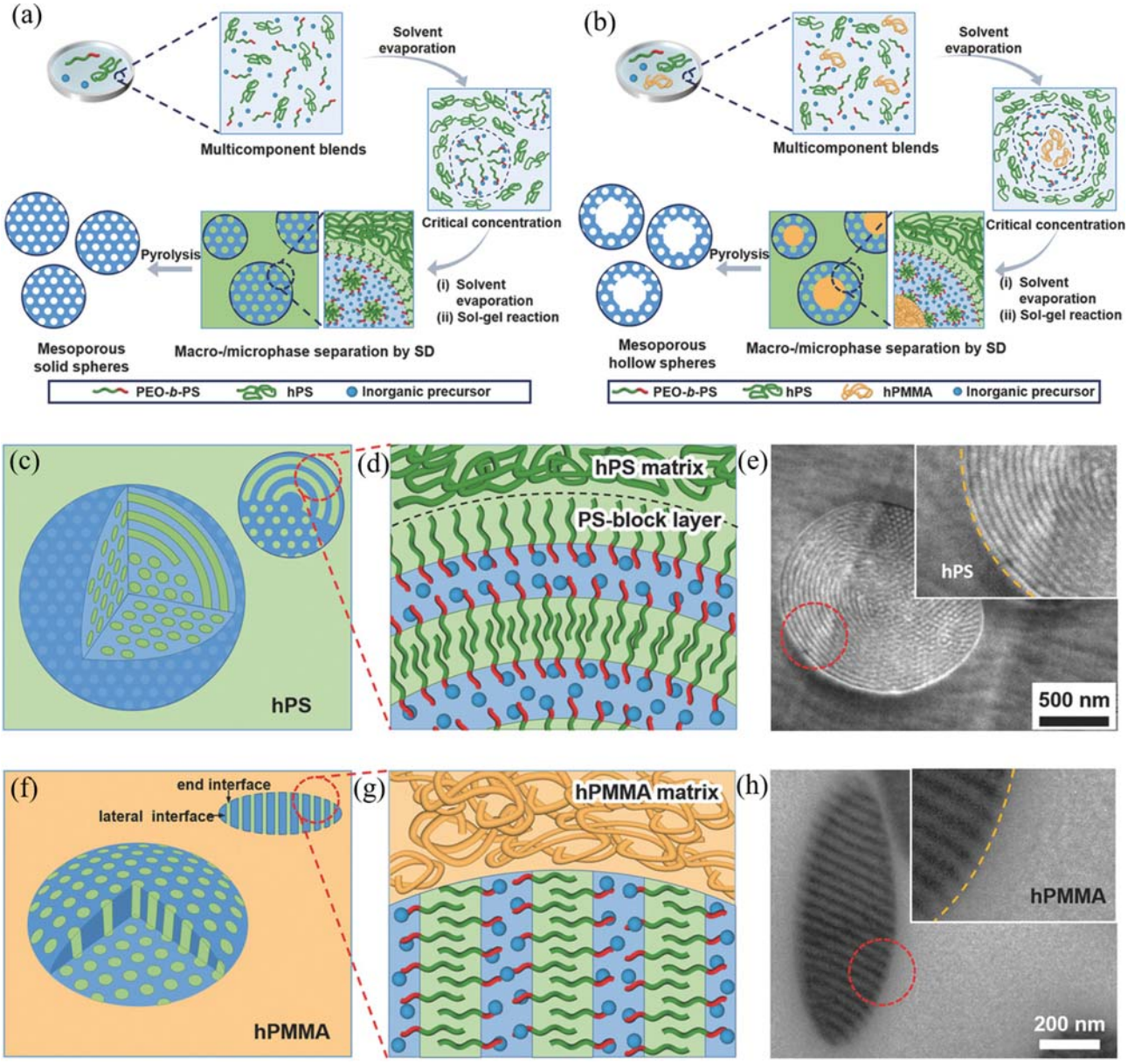

Fig. 3. Schematic representation of spherical and hollow assembly-based particle engineering (SHAPE) for (a) mesoporous spheres and for (b) mesoporous hollow spheres, ((c), (d)) schematics of BCP orientation at interface to hPS and (e) cross-sectional TEM image of as-made mesoporous aluminosilicate spheres confined in hPS matrix, ((f), (g)) schematics of BCP orientation at interface to hPMMA and (h) cross-sectional TEM image of as-made mesoporous aluminosilicate oblates confined in hPMMA matrix (Reprinted with permission from Ref. [65], Copyright 2018 John Wiley & Sons).

bic homopolymer (homopolystyrene (hPS) and homopolymethylmethacrylate (hPMMA)) with high molar mass (350 kg mol^{-1}) plays a decisive role in inducing macrophase separation without interfering with BCP-directed mesostructure formation. By simply adding excess hPS to the precursor/PEO-*b*-PS/THF solution, mesoporous spheres were formed during solvent evaporation. BCP-phase was confined within the excess hPS matrix and self-assembled toward the spherical morphology to decrease the total interfacial energy (Fig. 3(a)). In addition, the pore orientation and particle morphology were tuned by changing the kind of homopolymer matrix and associated enthalpic interactions at the interfaces. The hPS matrix provides an enthalpically favorable surface for PS block of BCP-phase, generating cylindrical nanochannel aligned parallel to the interfaces (Fig. 3(c)-(e)). On the other hand, hPMMA matrix provides an enthalpically neutral surface for both PEO and PS segments in the BCP-phase, creating vertically aligned cylindrical nanochannels (Fig. 3(f)-(h)). The anisotropic oblates were induced due to the lower interfacial energy of the end interface than lateral interface of BCP-domains. The particle size was easily controlled by tailoring the rate of solvent evaporation (*i.e.*, the faster the evaporation, the finer the macrostructure). The mesopore structure and size can be independently controlled by changing the relative amount of inorganic precursors and the molar mass of PEO-*b*-PS, respectively. As a result, this novel approach offers unprecedentedly high level of control over the pore size (15-50 nm), structure (lam, hex, bcc) and orientation (open, closed), the particle size (200 nm-5 μm) and morphology (sphere, oblate) as well as the chemical composition (silica, carbon, aluminosilicate, TiO_2, Nb_2O_5, and WO_3) [65].

Higher level of multicomponent co-assembly was further achieved by using binary homopolymer pairs (hPS and hPMMA) with various mass ratio as a matrix [65,67,68]. The multicomponent polymer blends can have a diverse blend morphology depending on their thermodynamic interactions at the interfaces, which are predicted by spreading coefficient and interfacial tension [69]. Kim et al. used such phase behavior as a rational tool for synthesis of inorganic mesoporous materials with tunable particle morphology (hollow sphere [65], anisotropic bowls [67] and nanosheets [68]). Major hPS and minor hPMMA pairs allowed preparation of mesoporous

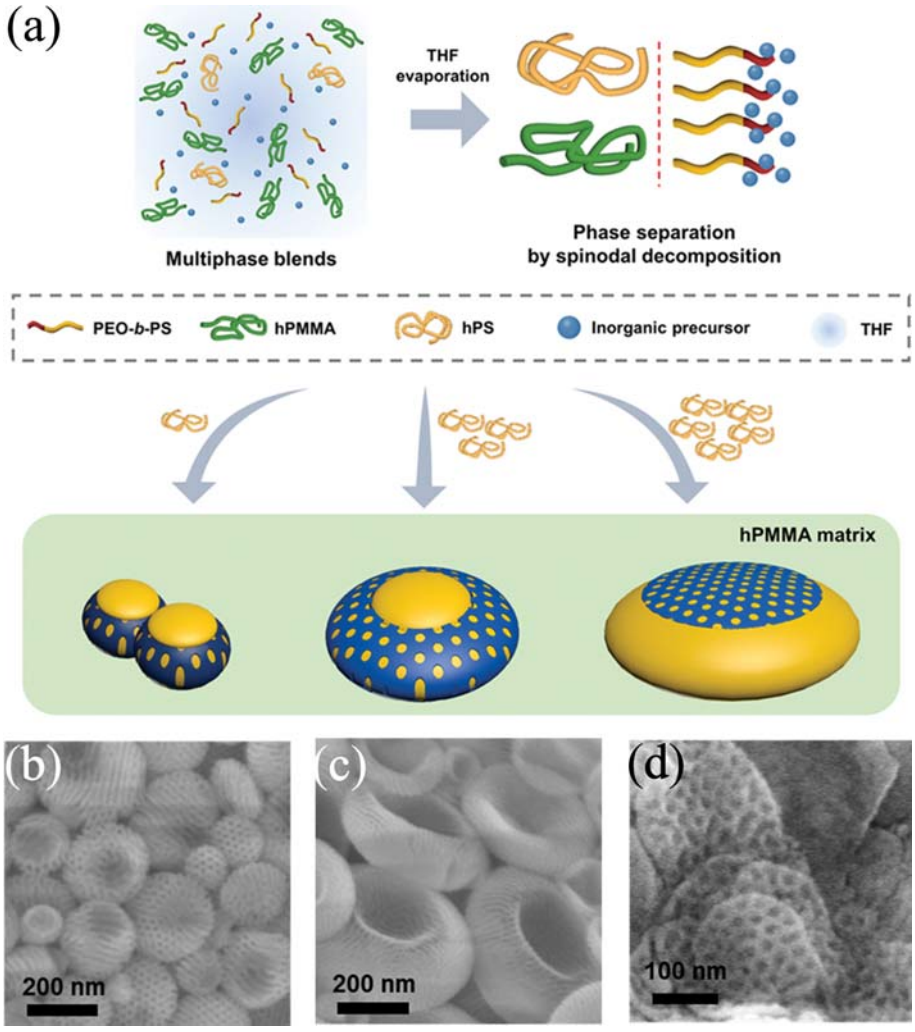

Fig. 4. (a) Schematic representation of anisotropically self-assembled particle (ASAP) approach, and SEM images of ((b), (c)) bowl-like mesoporous aluminosilicate particles with different particle/concavity sizes, and d) two-dimensional mesoporous aluminosilicate nanosheets (Licensed under CC-BY from Ref. [67]).

hollow spheres (Fig. 3(b)). In this case, BCP-phase intercalates at the hPS and hPMMA interface, resulting in formation of hPMMA@PEO-*b*-PS@hPS core shell morphology. When major hPMMA and minor hPMMA pairs were employed, a Janus type (hPS/PEO-*b*-PS)@hPMMA stack was formed (Fig. 4(a), (b)). PEO-*b*-PS phase partially covers hPS to reduce the relatively high energy hPS/hPMMA interfaces but cannot fully encapsulate hPS, because the difference in interfacial energy of hPS/hPMMA and PEO-*b*-PS/hPMMA is not significant [67]. Interestingly, as the amount of minor hPS increases, PEO-*b*-PS domains become thinner and wider to cover more hPS/hPMMA interfaces with fixed amount of PEO-*b*-PS, leading to simultaneous increase in concavity/particle sizes from 70/170 nm to 370/600 nm (Fig. 4(a)-(c)). At the optimum mass ratio of hPS and hPMMA, the PEO-*b*-PS phase spreads thinly to two-dimensional nanosheets with a thickness of a few nanometers (5-75 nm) (Fig. 4(a), (d)) [68]. Because the chemical composition/structure of the polymer and the interfacial tension are highly controllable, this polymer blend-directed multiscale assembly would enable the design of various macrostructure-controlled mesoporous materials with a high degree of structural/morphological diversities.

LITHIUM-ION BATTERIES

1. Mesoporous Materials for Lithium-ion Battery Applications

LIBs store and release energy by converting electric energy into chemical energy and vice versa. Electroactive materials in LIBs have their own Li ion insertion/extraction reaction potential, capacity, and stability [3,5,70]. Therefore, the combination of anode and cathode electrode materials mainly determines the battery's power/energy density and cycle life. Since the first commercial release of LIB (graphite//$LiCoO_2$) by Sony in 1991, the energy density and cycle life of LIBs have been significantly improved, and LIBs are currently applied in numerous applications including portable devices, large scale grid energy storage, and electric vehicles.

As LIBs consumption grows, consumers have requested more specialized batteries for their applications, such as miniature batteries, rapid charge/discharge batteries, high energy density batteries regardless of cell's size, and long cycle life batteries with moderate energy density. Therefore, researchers have investigated various approaches to developing advanced electrode materials over the past few decades. Among various approaches, in this chapter, we will summarize recent progress in mesoporous materials for LIB applications and clarify research challenges of mesoporous materials for better energy storage performance. In general, commercial LIBs use ~10 μm sized spherical anode (graphite) and cathode (*e.g.*, lithium cobalt oxide, lithium iron phosphate, and lithium nickel cobalt manganese oxide) particles as active materials. Mesoporous materials have different morphologies compared to these commercial particles but have characteristic advantages as already described in the introduction. We will cover the merits of mesoporous electrode materials depending on Li^+ reaction mechanisms: i) intercalation, ii) conversion, iii) alloying mechanisms and hybridization of these reaction mechanisms.

2. Intercalation Electrode Materials

Commercial LIBs utilize the intercalation mechanism which inserts/extracts Li ions into the void space in the crystal structures

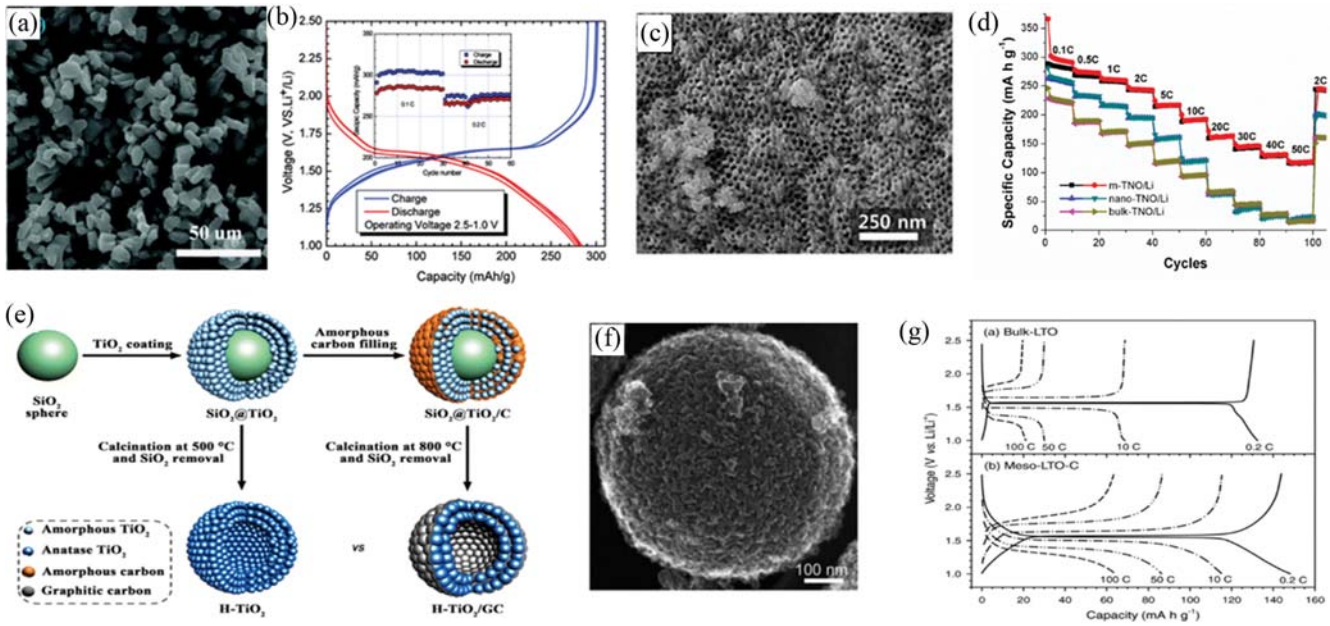

Fig. 5. (a) SEM image of $TiNb_2O_7$ synthesized by solid-state reaction and (b) its charge/discharge profiles and cycle performance (inset) (Reprinted with permission from Ref. [71], Copyright 2011 American Chemical Society), (c) SEM image of mesoporous $TiNb_2O_7$ (m-TNO) and (d) capacities at different C-rates (Reprinted with permission from Ref. [41], Copyright 2014 American Chemical Society), (e) Schematic illustration of the graphitic carbon coated mesoporous TiO_2 hollow spheres (Reprinted with permission from Ref. [72], Copyright 2015 American Chemical Society), (f) SEM images of spherical mesoporous TiO_2-Bronze (Reprinted with permission from Ref. [73], Copyright 2011 John Wiley & Sons), and (g) charge/discharge profiles of bulk-$Li_4Ti_5O_{12}$ and mesoporous-$Li_4Ti_5O_{12}$-C composites (Reprinted with permission from Ref. [74], Copyright 2011 John Wiley & Sons).

or defect sites [75,76]. Intercalation reaction accompanies crystal structure change but does not break the chemical bonding in the host materials. Therefore, intercalation reaction makes small volume change and exhibits very stable cycling performance compared to that of high capacity materials using conversion or alloying reaction mechanisms. However, the number of Li^+ intercalations into the void space is usually limited to ≤1, resulting in low theoretical capacities and energy densities.

Mesoporous materials have high electrode/electrolyte interface area and small crystallite size (less than tens of nanometers). Also, the structure exposes high portion of crystallite edge and defect sites to the electrolyte. Therefore, intercalation materials with mesoporous structures have shown interesting intercalation processes; compared to the same materials in the bulk form, mesoporous electrode materials exhibited increased reversible capacities and different charge/discharge profiles in the electrochemical systems. It is well known that nanosizing and high surface area accelerate the Li^+ insertion process, which is by the transition of reaction mechanism from diffusion controlled intercalation into capacitor like intercalation process [77-79] (see further in Li-HSC section). Although it has lower electrode packing densities, a mesoporous structure can provide higher reversible capacity and better rate performance compared to those of commercial bulk powder. Therefore, mesoporous structured materials require fewer active materials to fabricate LIBs which are irrelevant to the size.

In general, commercial intercalation materials have poor rate performance due to the poor electronic and ionic conductivity and large crystallite size (long solid state diffusion length). However, mesopores can soak the electrolyte, which makes a broad Li^+ entrance area and provides a fast supplement of Li^+ after intercalation process. In addition, mesoporous materials have short solid-state diffusion length, which is related to the reaction time constant τ ($\tau = L^2/2D$, L is diffusion length and D is diffusion coefficient) [80,81]. Therefore, mesoporous structure can achieve a rapid charge/discharge process compared to bulk materials.

As an example, the Goodenough group reported $TiNb_2O_7$ (TNO) as a new intercalation anode material in 2011 (Fig. 5(a)-(b)) [71, 82]). Its theoretical capacity (387.6 mAh g^{-1}) is higher than that of other Ti-based intercalation materials (anatase TiO_2: 168, TiO_2(B): 335, and $Li_4Ti_5O_{12}$: 175 mAh g^{-1}, respectively). They synthesized the material with a solid state reaction method in 900-1,100 °C range. With 1.0 V (*vs.* Li/Li^+) cut-off, bulk TNO delivered 285 mAh g^{-1} of reversible capacity at 0.1 C but poor rate performance, ~230 mAh g^{-1} at 0.2 C. In 2014, the Dai group [83] and the Lee group [41] reported block copolymer derived synthesis and anode applications of mesoporous structured TNOs (m-TNOs), respectively. The Dai group prepared m-TNO using a commercially available F127 polymer. The m-TNO with 20-30 nm pores showed high reversible capacity (281 mAh g^{-1}) and fast charge/discharge performance at 50 C (128 mAh g^{-1}). They also investigated the reaction mechanism of m-TNOs using *in-situ* X-ray scattering and X-ray absorption spectroscopy. In parallel, the Lee group applied a lab-made block copolymer, PEO-*b*-PS, as a structure directing agent, m-TNO, constructed of 15 nm crystals and 40 nm pores, delivered 289 mAh g^{-1} at 0.1 C rate and 162 mAh g^{-1} at 20 C rate (Fig. 5(c)-(d)). Both papers proved that mesoporous structures provide an excellent rate performance. Besides, the Lee group recently reported that hierarchically porous structures containing both mesopores and macropores (>50 nm pores) can achieve improved ion diffusion process, resulting in better rate capability compared to the same materials with only mesopores [42,63]. These results indicate that well-controlled porosity is an important factor for enhancing the rate performance of intercalation materials. On the other hand, m-TNOs can be simply synthesized by other approaches. Yang et al. applied solvothermal reaction method to synthesize m-TNOs with carbon coated structure [84]. With conductive carbon layer on low conductivity m-TNO surface, they improved charge/discharge rate performance, 200 mAh g^{-1} at 30 C rate in m-TNO/C *vs.* 132 mAh g^{-1} in pure m-TNO. By analyzing cyclic voltammetry curves, they claimed m-TNO structure has high portion of capacitive reaction and it was enhanced after carbon coating process. Besides, m-TNOs with different material compositions were also prepared for LIB applications by the facile solvothermal method [85-87].

Mesoporous structures were also applied to titanium based intercalation anode materials. Because of high reaction potential (above 1.0 V *vs.* Li/Li^+), Ti-based materials are actively investigated in high-power battery applications because there is no risk of Li metal formation problem during the cycling [88,89]. The Sun group reported F^- ion doped mesoporous TiO_2 by hydrothermal synthesis [90]. The TiO_2 nanoclusters have ~1 μm size and ~7 nm pores, formed by the agglomeration of nanoparticles. In this study, addition of F^- ion increased specific surface area, pore size, and pore volume. Therefore, the F-doped m-TiO_2 electrode showed 144 mAh g^{-1} at 30 C rate, but ~50 mAh g^{-1} in pristine TiO_2. The Maier group also synthesized spherical and sub-micrometer sized TiO_2-$CdSO_4$ particles using a solution phase synthesis method and selectively removed $CdSO_4$ phase, resulting in formation of mesoporous structured TiO_2 [91]. The mesoporous TiO_2 electrode delivered high reversible capacity up to $Li_{0.63}TiO_2$ (210 mAh g^{-1}). Therefore, they proved mesoporous structure can exceed the theoretical capacity limitation (0.5 Li^+ insertion into anatase TiO_2, 168 mAh g^{-1}). On the other hand, the Wang group reported hollow TiO_2/graphitic carbon (H-TiO_2/GC) material (Fig. 5(e)) [72]. They hydrolyzed titanium precursors on the surface of SiO_2 sphere and applied glucose as a carbon source for carbon coating process. Due to the high surface area and porous structure, the electrode exhibited ~178 mAh g^{-1} at 100 mA g^{-1} current density and ~137 mAh g^{-1} at 1 A g^{-1} (up to 1,000 cycles). Liu et al. reported synthesis of mesoporous TiO_2(B) spheres by converting TiO_2/silica spheres, prepared by ultrasonic spray pyrolysis, into TiO_2(B) using sodium hydroxide solution treatment (Fig. 5(f)) [73]. As an anode material, the mesoporous TiO_2(B) achieved a maximum capacity of 256 mAh g^{-1} at 0.1 C and 130 mAh g^{-1} at 10 C, respectively.

In addition to TiO_2 materials, various mesoporous structures have been applied to improve the capacity and rate performance of $Li_4Ti_5O_{12}$ (LTO) materials [74,92-94]. Kang et al. synthesized mesoporous LTO-C composite and tested anode performance (Fig. 5(g)) [74]. Using galvanostatic charge/discharge, they showed excellent rate performance in mesoporous active material electrode, compared to that of bulk LTO electrode. Electrochemical impedance spectroscopy test on LTO symmetric cell proved mesoporous structured LTO-C materials has smaller charge transfer resistance, indi-

cating better ion/electron diffusion processes. Besides, mesoporous structures have improved electrochemical performance in different types of active materials such as Nb_2O_5 [95-97], MoS_2 [98], and even cathode materials ($LiMn_2O_4$ [99-101], $LiFePO_4$ [102-104], $LiCoO_2$ [105], etc.).

3. Conversion Electrode Materials

Some metal anion compounds (M_aX_b, M=transition metal and X=anion), such as metal oxides, sulfides, nitrides, fluorides, and phosphides, react with Li^+ by conversion reaction processes [112-114]. During this reaction, the bonding in metal anion is disconnected and anion forms Li-X compounds leaving metal phase. Depending on the oxidation state of metal, metal anion compounds can deliver multiple Li^+, resulting in high capacity from 500 to 1,200 mAh g^{-1}. Therefore, conversion materials have been considered as next generation high energy electrode materials. However, conversion reaction accompanies large volume change during the decomposition of metal anion compounds and formation of new Li-X compounds. Also, this Li-X usually has very low electrical con-

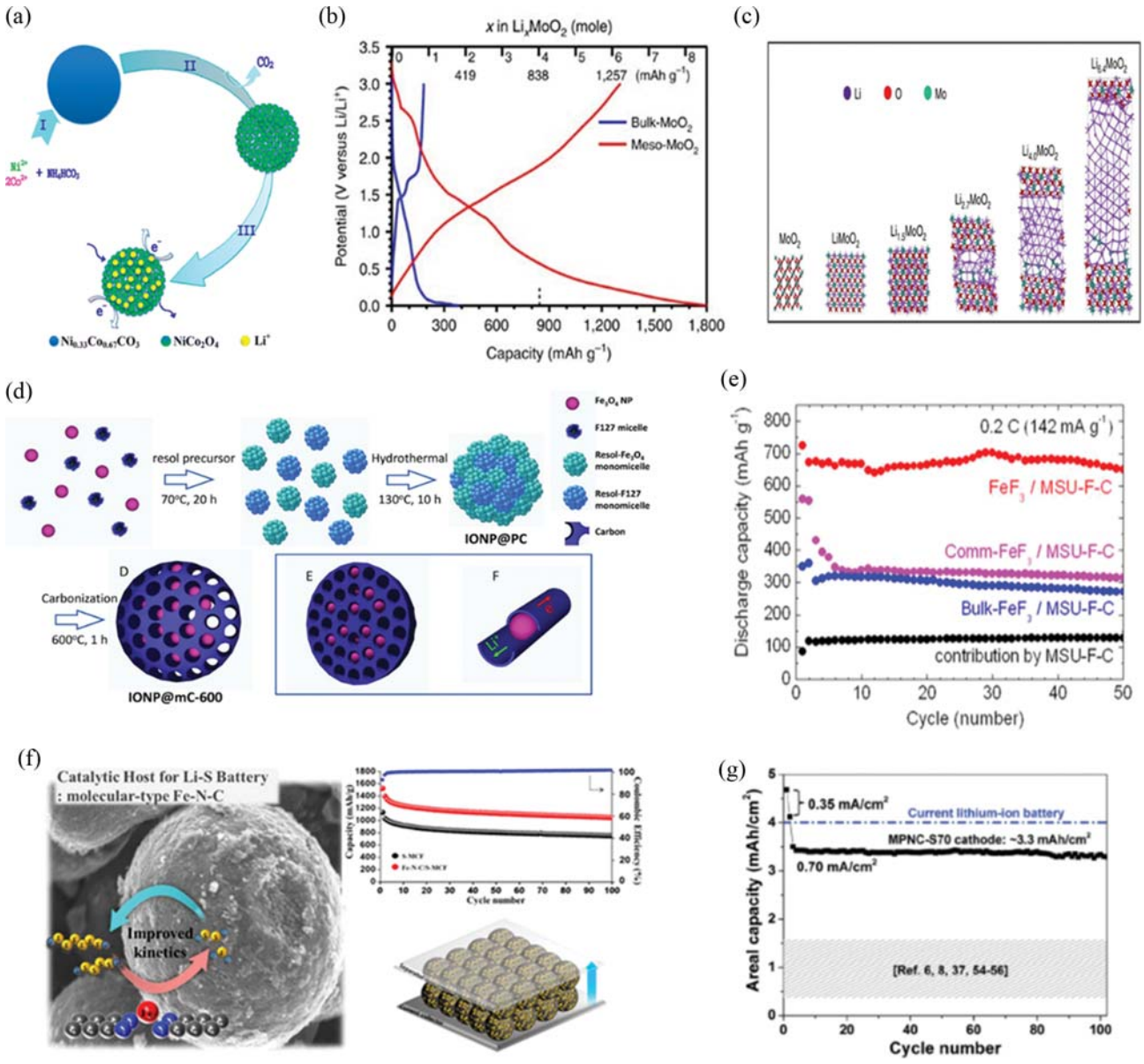

Fig. 6. (a) Schematic illustration of the formation of mesoporous $NiCo_2O_4$ (Reprinted with permission from Ref. [106], Copyright 2013 American Chemical Society), (b) exceptional capacity in mesoporous MoO_2 compared to bulk-MoO_2 electrode, (c) Li metal formation between lithiated MoO_2 layers in mesoporous structure (Licensed under CC-BY from Ref. [107]), (d) synthesis of mesoporous Fe_3O_4/carbon composite (Reprinted with permission from Ref. [108], Copyright 2013 John Wiley & Sons), (e) cycle stability of FeF_3/mesoporous carbon, commercial FeF_3, Bulk-FeF_3 and mesoporous carbon physical mixture electrodes (Reprinted with permission from Ref. [109], Copyright 2016 American Chemical Society), (f) Fe-N-C catalyst coated spherical mesoporous carbon for Li-S batteries (Reprinted with permission from Ref. [110], Copyright 2018 American Chemical Society), and (g) N-doped mesoporous carbon/sulfur composite electrode with high areal capacity (Reprinted with permission from Ref. [111], Copyright 2013 John Wiley & Sons).

ductivity. Therefore, these two factors make a short cycle life due to the pulverization from the electrode layer and increase in electrode resistance by the agglomeration of Li-X phase. Besides, most anode materials react with Li^+ at lower potential (<1 V *vs.* Li/Li^+), which makes repetitive solid-electrolyte interphase (SEI) formation during the volume change. Lastly, intrinsic reaction processes have a large charge/discharge overpotential so that conversion materials show low energy efficiency in spite of high reversible capacity. Therefore, conversion materials have issues to be addressed, such as alleviation of volume change, improvement of electrical conductivity, and formation of highly dispersed matrix for metal and Li-X phases.

Volume change during Li^+ insertion/extraction processes leads to structural collapse, increase in electrode thickness, and even pulverization from the electrode. After first cycle, the size of conversion materials and electrode thickness cannot be recovered to initial states. It thus induces low electrode density and a sharp increase in contact resistance. To solve this volume change issue, researchers incorporated conversion materials into mesoporous structures. For example, Li et al. prepared monodisperse $NiCo_2O_4$ mesoporous microspheres by two-step synthesis [106]; i) solvothermal reaction to form spherical $Ni_{0.33}Co_{0.67}CO_3$ precursor and ii) calcination in air to create mesopores by the release of CO_2 gas (Fig. 6(a)). Due to the porous structure, the anode reached ~1,200 mAh g^{-1} with excellent cycle stability. Similar to this paper, solvothermal technique has been widely applied in the synthesis of conversion materials with mesoporous structures and spherical particle morphology [115,116].

Hard template route was also applied to design highly ordered mesoporous conversion materials [117-119]. KIT-6 silica templated-metal oxides or sulfides were prepared and applied as anode material applications. Mesoporous materials have high surface area (50-150 m^2 g^{-1}), bimodal pores (~4 and ~20 nm), and exhibit improved capacity and cycle stability compared to the bulk materials [117-119]. Wen et al. controlled the porosity of ordered mesoporous $CuCo_2O_4$ materials by using KIT-6 templates synthesized at different temperature [120]. By controlling hydrothermal reaction temperature at 40 and 130 °C, they prepared two KIT-6 silica templates with different pore sizes. Interestingly, KIT-6 prepared at 40 °C filled precursor into one of bimodal pores, while precursors were fully impregnated in both pores in KIT-6-130 °C sample. As a result, m-$CuCo_2O_4$ material prepared by KIT-6-40 °C has larger mesopores, high surface area and high reversible capacity at all current densities. On the other hand, Yoon and coworkers prepared m-CuO and m-MoO_2 materials [107,121]. In addition to confirming the enhanced electrochemical performance, they applied computational modeling, X-ray diffraction, X-ray absorption spectroscopy, and TEM tools to investigate different reaction mechanisms in the mesoporous structures. They made an exciting discovery in m-MoO_2 material, which shows exceptional capacity of 1,814 mAh g^{-1}, more than twice its theoretical capacity [107]. They proved the origin of this additional capacity is due to the contributions from Li^+ intercalation reaction and formation of a metallic Li-rich phase between Li^+ intercalated MoO_2 phase (Fig. 6(b)-(c)). This study provides a meaningful finding that the nanoengineering not only improves battery performance but also makes a new Li^+ reaction mechanism.

On the other hand, to increase electrical conductivity of the electrode, researchers have made mesoporous structured conductive materials. Mesoporous carbon is the most representative conductive host material because it has high surface area (>1,000 m^2 g^{-1}), large pore volume (>1 cm^3 g^{-1}), and rigid scaffold [122]. For example, iron oxides are very cheap and high capacity materials (Fe_2O_3: 1,007 mAh g^{-1} and Fe_3O_4: 926 mAh g^{-1}) but have poor cycle performance due to the volume change problem. Therefore, nanosized Fe_xO_y particles were loaded inside the mesoporous carbon matrix (Fig. 6(d)). The carbon matrix acts as an electron pathway and prevents swelling and structural failure. As a result, the iron oxide/carbon composites showed improved cycle life and enhanced rate capability [108,123,124]. Jo et al. synthesized ordered mesoporous tungsten oxide carbon composite [48]. On the contrary to active materials in the host materials, they constructed mesoporous structure by using self-assembly of structure directing agent with both tungsten and carbon precursor. Carbon precursor was decomposed into amorphous carbon phase and prevented agglomeration of tungsten oxide particles. Therefore, this structure shows fine composite structure such as ~2 nm crystallites/amorphous carbon, 48 m^2 g^{-1} surface area, 0.2 cm^3 g^{-1} pore volume, ~10 nm nanowalls, and 30 nm pores. In comparison with m-WO_3 having almost identical mesoporous structure but large crystallites (6-10 nm) and no carbon phase, the composite material showed higher capacity, smaller internal resistance, and even better reversibility, as confirmed by galvanostatic charge/discharge, galvanostatic intermittent titration technique, and X-ray absorption spectroscopy.

In addition to anodes, conversion type cathode materials can be impregnated inside porous carbon structures. Chun at el. reported ammonium fluoride mediated synthesis to prepare metal fluoride particles in mesoporous carbon materials [109]. Metal fluorides are Li-free cathode materials which have high theoretical capacity between 500 and 800 mAh g^{-1}. Ammonium fluoride (NH_4F) is decomposed into NH_3 and HF gases at ~100 °C. Therefore, metal precursor loaded mesoporous carbon reacts with NH_4F, resulting in formation of CuF_2, FeF_3, CoF_2 and carbon composites. These metal fluoride/carbon composite exhibited highly improved reversible capacity, cycle life, and even decreased charge/discharge overpotential, compared to the bulk materials (Fig. 6(e)). Different types of metal fluoride materials can also be synthesized by solvothermal methods [125,126]. Lithium sulfur (Li-S) batteries, the most representative next generation batteries, also use conversion type sulfur cathode materials. After revisiting the Li-S system using ordered mesoporous carbon/sulfur composite by the Nazar group [127], mesoporous carbon materials with different particle morphologies, pore sizes, surface area, surface functionalities, and even composite structures were introduced into Li-S stabilization research [128-130]. Recently, Li-S battery fields have focused on increasing sulfur loading inside the mesoporous matrix and modifying surface of mesoporous materials to achieve practical active material loading, fast conversion kinetics, and stable cycling performance (Fig. 6(f)-(g)) [110,131-134].

4. Alloying Electrode Materials

Alloying materials react with Li^+ by forming Li-metal alloy and have high theoretical capacity but suffer from large volume change-

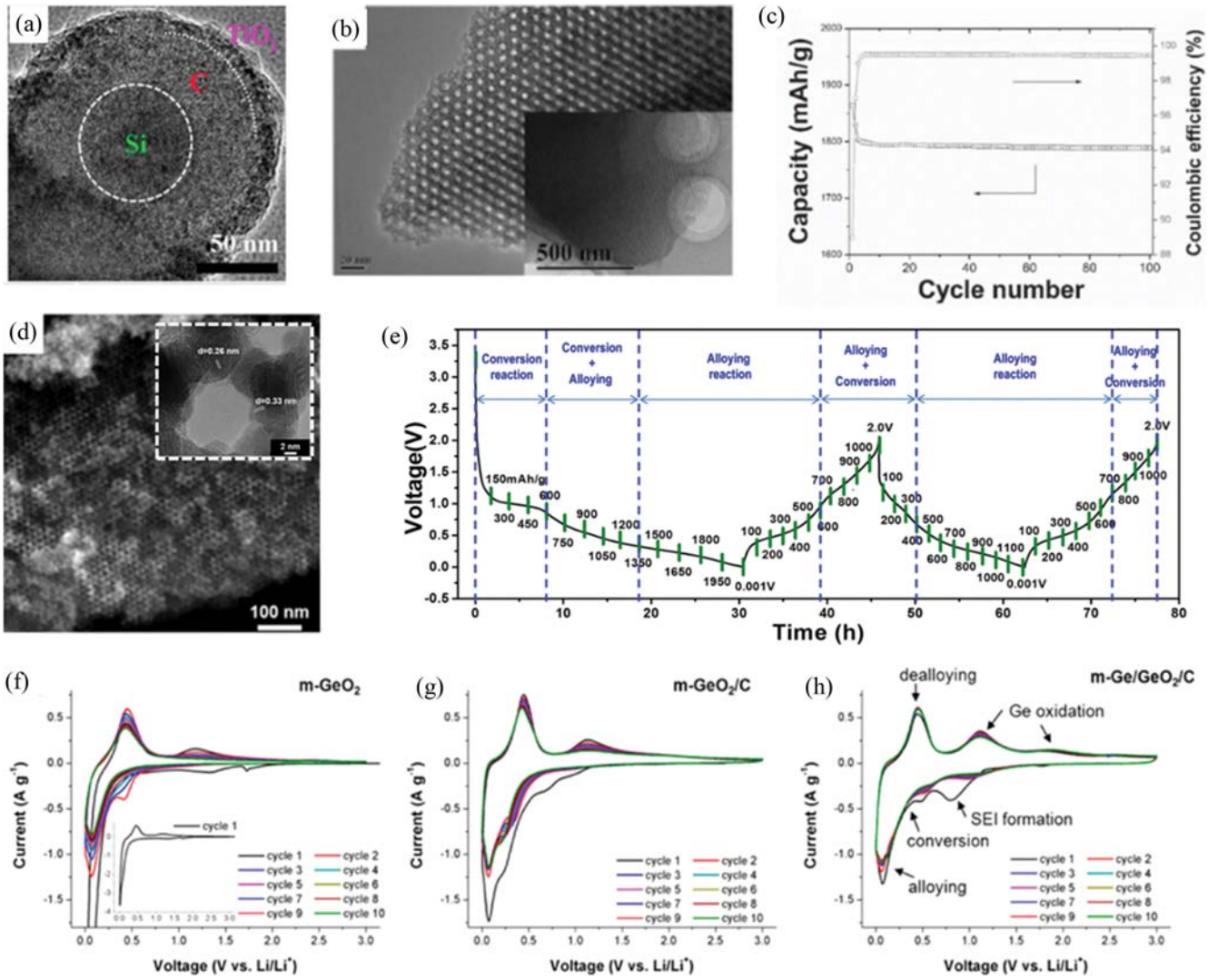

Fig. 7. (a) TEM image of Si-mesoporous carbon-TiO_2 composite (Reprinted with permission from Ref. [135], Copyright 2016 American Chemical Society), (b) TEM image of ordered mesoporous Si and C composite and (c) its cycling performance (Reprinted with permission from Ref. [136], Copyright 2014 John Wiley & Sons), (d) SEM image of mesoporous SnO_2 (inset: TEM image) and (e) diagram of overall electrochemical reaction mechanism of m-SnO_2 (Reprinted with permission from Ref. [137], Copyright 2014 American Chemical Society), and (f)-(h) cyclic voltammetry curves of m-GeO_2 (f), m-GeO_2/C (g), and m-Ge/GeO_2/C (h) (Reprinted with permission from Ref. [47], Copyright 2015 American Chemical Society).

related problems, similar to conversion materials [138]. Among alloying materials (Si, Sn, Sb, Ge, etc.), Si has been most actively investigated for high capacity anode applications because of its high reversible capacity (>3,500 mAh g^{-1}), natural abundance, and versatility in various industrial fields [139]. After Si nanowire study for anode application by the Cui group in 2008 [140], nanostructuring researches for Si have grown explosively. It is well known that a few tens of Si nanoparticles have resistance to fracture and rapid Li^+ insertion/extraction kinetics [141-143]. The Cho group synthesized nanosized Si inside ordered mesoporous carbon using Si-C_4H_9 precursor. The composite electrode exhibited 87% capacity retention (2,738 mAh g^{-1}) after 80 cycles [144]. Yang and coworkers fabricated Si@C@TiO_2 core-shell-shell structure (Fig. 7(a)) [135]. They coated Si particles with mesoporous carbon shell which acts as electron pathway and buffers volume for Si expansion. TiO_2 layer on carbon shell provides a rigid protective layer and forms stable SEI layer, achieving 1,010 mAh g^{-1} after 710 cycle. Zhao and coworkers simply prepared mesoporous Si/C materials and showed 1,864 mAh g^{-1} at first cycle and 1,790 mAh g^{-1} at 100th cycle (Fig. 7(b)-(c)) [136]. Triconstituent co-assembly of pluronic triblock copolymer with resol (carbon source) and tetraethyl orthosilicate (silica source) led to formation of ordered mesoporous SiO_2/C composites. In turn, SiO_2 was directly converted to Si by magnesiothermic reduction without forming SiC phase. Likewise, various mesoporous Si structures were prepared by reducing mesoporous SiO_2 structure through Mg reduction process [145,146].

On the other hand, other types of alloying materials have also been impregnated inside mesoporous host materials. Sn nanoparticles confined in porous carbon host showed greatly enhanced capacity and cycling performance [147,148]. For example, BCP-

directed co-assembly allowed selective positioning of carbon and Sn metal; Sn nanoparticles or wires were confined inside mesostructured carbon [36]. Ge particles, which have high capacity, high Coulombic efficiency, and high ionic conductivity, were also loaded inside mesoporous carbon host materials [149-151].

Transition metal anion (M_aX_b) compounds containing alloying metals (Zn, Sn, Ge, etc.) can store Li^+ by the combination of conversion and alloying reactions [152]. Initially, metal anion compounds react with Li^+ by forming Li-X compounds with transition metal, followed by alloying reaction. The Kim and Yoon groups investigated the reaction mechanism for ordered mesoporous SnO_2 electrode using synchrotron-based X-ray analysis [137,153]. The m-SnO_2 electrode showed highly enhanced reversible capacity, 1,043 mAh g^{-1}, which surpassed other SnO_2 studies. They applied X-ray absorption spectroscopy and X-ray diffraction to understand th reaction mechanism in ordered mesoporous structure. It was confirmed that conversion reaction occurs earlier in the first lithiation, followed by conversion/alloying reactions and alloying process at lower voltage. From first de-lithiation, alloying reaction takes place at lower reaction potential and both conversion/alloying reactions happen at relatively high reaction potential (Fig. 7(d)-(e)). This hybrid reaction mechanism is also found in Ge/GeO_2/C composite electrodes. In mesoporous Ge/GeO_2/C composites, carbon phase provides a facile electron conduction and Ge acts as a catalyst for Ge oxidation process. Therefore, the composite electrodes showed high reversibility, stable cycle life, and direct evidence for characteristic Ge re-oxidation (Fig. 7(f)-(h)) [47,154]. Other metal anion compounds, such as metal phosphide, sulfide, and their mixture, were also prepared into mesoporous structures and achieved high capacity, stable cycle performance, and improved reversibility [155-158].

LITHIUM-ION HYBRID SUPERCAPACITORS

1. Mesoporous Materials for Lithium-ion Hybrid Supercapacitor Applications

Supercapacitors (SCs), including electric double layer capacitors (EDLCs, Fig. 8(a)) and pseudocapacitors (PCs, Fig. 8(b)), have been used in electrical applications. However, because SCs store charges through (i) the physisorption of electrolyte ions on the surfaces of a charged electrode material (EDLC) and (ii) the surface and/or near-surface redox reactions (PC), SCs deliver lower energy compared to LIBs [159,161,162]. Hence, their use has been limited to specific applications requiring fast charge/discharge rates and long cycle life.

To solve the fatal shortcomings of SC, hybrid energy storage systems have been intensively developed with a new concept called "lithium-ion hybrid supercapacitor" (Li-HSC) proposed by Amatucci et al. [163] In general, Li-HSC is composed of LIB anode and SC (especially EDLC) cathode. For example, LIB electrodes such as graphite, $Li_4Ti_5O_{12}$ (LTO) and anatase TiO_2 are commonly used as anodes while carbon material-based EDLC electrodes are used as cathodes for Li-HSC in organic electrolytes containing Li salts (Fig. 8(c)) [164-167]. Thus, Li-HSC stores charge with different electrochemical reactions based on Faradaic reactions at the anode and non-Faradaic reactions at the cathode. Due to these unique properties, Li-HSC simultaneously provides excellent power capability and high energy with long-term cycling. However, the difference in kinetics between LIB anode (slow) and EDLC cathode (fast) due to different charge storage mechanisms is one of the biggest problems in the Li-HSC research community [165].

To improve the anode kinetics, various anode candidates for Li-HSC such as LTO, Nb_2O_5, and Li_3VO_4 have been studied by introducing electrode engineering in the nanoscale domain [168]. Among the various nano-sized electrode materials for Li-HSC, we introduce the advantages of porous materials, including metal oxides and carbonaceous materials, especially as Li-HSC anodes.

2. Metal Oxide Materials

Since the first report on Li-HSC in 2001, anatase TiO_2 and LTO have been commonly used as materials for Li-HSC systems [163, 172]. In particular, LTO studies are much more advanced than those of anatase TiO_2 due to the attractive electrochemical behavior of LTO: (i) Theoretical capacity (~175 mAh g^{-1}) at safe operating voltage (~1.55 V *vs.* Li/Li^+, possible to 1.0 V cut-off) with little electrolyte decomposition [173], (ii) fast charge/discharge rate (high rate capability) [74] and (iii) zero-strain Li^+ insertion/extraction characteristics with little volume change during cycling [174]. Also, due to the LTO's operating voltage (above 1.0 V compared to Li/Li^+), LTO-based Li-HSC can utilize low-cost, lightweight Al current collectors for anodes instead of expensive and heavy Cu current collectors [175]. Amatucci and coworkers for the first time demonstrated that nanostructured LTO anodes synthesized by

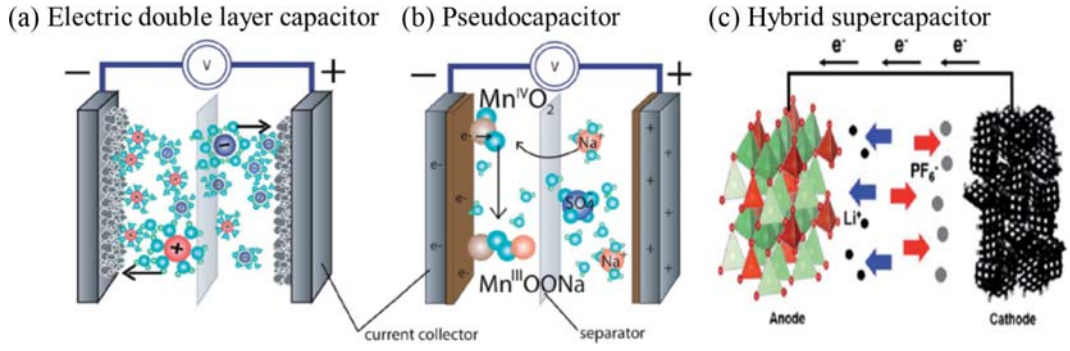

Fig. 8. (a) Schematic illustration for (a) electric double layer capacitor, (b) pseudocapacitor, (Reprinted with permission from Ref. [159], Copyright 2013 Royal Society of Chemistry), and (c) lithium-ion hybrid supercapacitor (Reprinted with permission from Ref. [160], Copyright 2017 Royal Society of Chemistry).

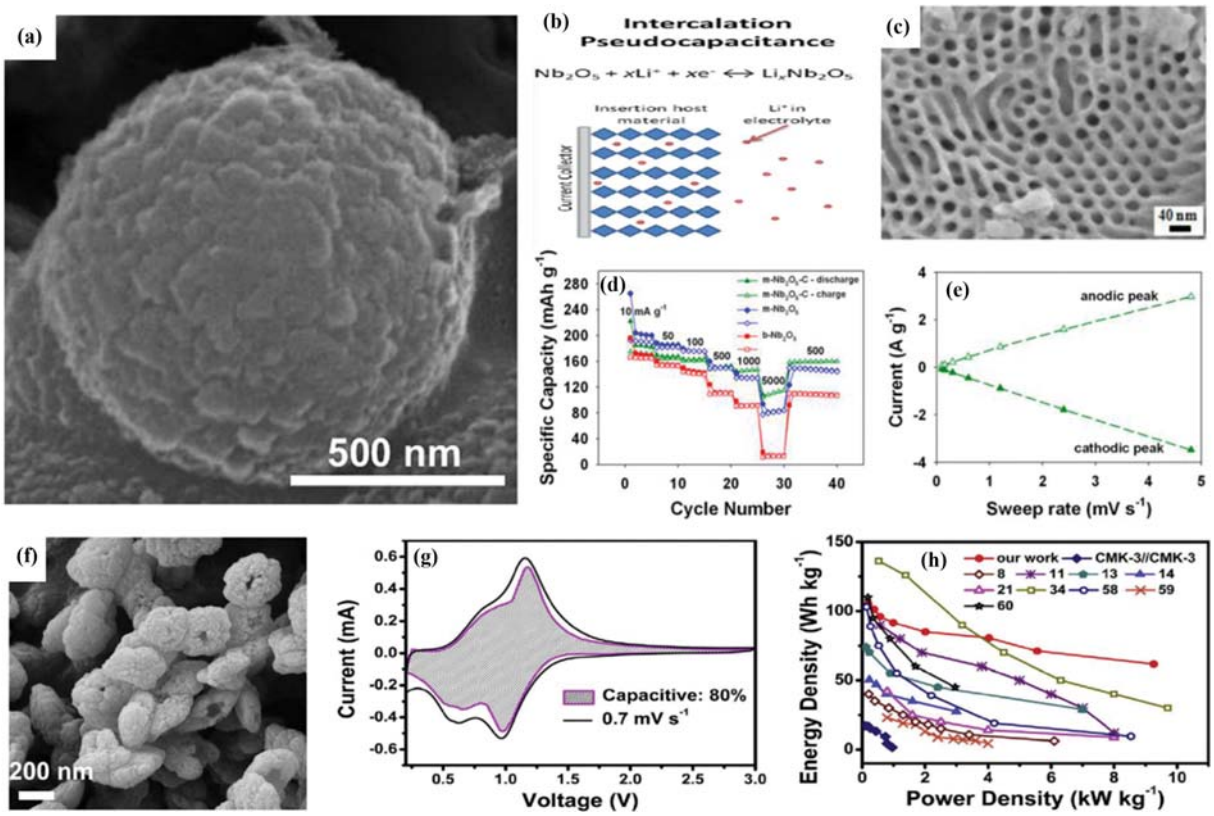

Fig. 9. (a) SEM image of C-LTO (Reprinted with permission from Ref. [169], Copyright 2013 Elsevier), (b) schematic illustration on intercalation pseudocapacitance (Reprinted with permission from Ref. [79], Copyright 2014 Royal Society of Chemistry), (c) SEM image of m-Nb_2O_5-C, (d) Rate capability comparison on m-Nb_2O_5-C, m-Nb_2O_5, bulk-Nb_2O_5, (e) specific peak current of m-Nb_2O_5-C on various scan rates (Reprinted with permission from Ref. [170], Copyright 2014 American Chemical Society), (f) SEM image of hp-LVO/C, (g) CV curve of hp-LVO/C with separation between the total current (solid line) and capacitive current (shaded region), and (h) Ragone plots of hp-LVO/C and other results previously reported (Reprinted with permission from Ref. [171], Copyright 2018, Elsevier).

high temperature solid-state reaction can be used for Li-HSCs [163]. They showed that the energy of a prototype Li-HSC packed cell using an LTO anode is achieved at ~20 Wh kg^{-1} with a fairly stable cycle performance (capacity retention: ~94% over 4,000 cycles, similar to that of conventional SC and better than that of LIB). After Amatucci et al's report, various nanostructured LTO anodes have been reported to further enhance the electrochemical properties of LTO [168,176]. In particular, mesostructured LTO electrode materials have been studied extensively for Li-HSC applications because they offer a variety of advantages, as mentioned in the introduction and LIB section. For example, the Sun group reported that carbon-coated micron-sized LTO spherical particles (C-LTO, Fig. 9(a)) with well-defined mesopores (3-10 nm pore diameter range) synthesized by hydrothermal method could be used as excellent Li-HSC anodes [169]. The specific capacity and rate performance of the prepared C-LTO was ~165 mAh g^{-1} at current of 0.17 A g^{-1} (1 C) and ~142 mAh g^{-1} at current of 8.5 A g^{-1} (50 C), which is an excellent rate capacity (Li half-cell data). In addition, the Li-HSC full cell data showed high energy (~36 Wh kg^{-1}) and fast charge/discharge rate (~1,600 W kg^{-1}) behavior, and stable cycling performance for 1,000 cycles in the operating voltage range from 1.5 to 2.5 V.

Recently, the development of a new Li-HSC anode instead of the conventional LTO-based anode has been recognized as a major challenge in the field of Li-HSC research. This is because the LTO suffers from the low theoretical capacity (~175 mAh g^{-1}) and narrow operating voltage range (~1.55 V *vs.* Li/Li^+), which is translated into low energy (E), considering $E=1/2CV^2$ (where C=capacitance, V=operating voltage). To overcome this limitation, many researchers have proposed a new Li-HSC anode. In particular, the Dunn group strongly proposed Nb_2O_5 as a promising Li-HSC anode to further improve the energy-related Li-HSC electrochemical performance [177,178], because of higher theoretical capacity of Nb_2O_5 (~200 mAh g^{-1}) than that of LTO. Nb_2O_5 also stores charge in a very short time because there is no limitation of solid diffusion, mainly due to the inherent charge storage mechanism called intercalation pseudocapacitance (Fig. 9(b)) [79,179]. However, in order to maximize the electrochemical properties of Nb_2O_5, an increase in electronic conductivity and control over the crystal structures (desirably orthorhombic phase) is highly required [180,181]. Lim et al. synthesized a highly ordered mesoporous orthorhombic Nb_2O_5/carbon nanocomposites (m-Nb_2O_5-C, Fig. 9(c)) using a lab-made block copolymer, PEO-*b*-PS, and applied it as a new Li-HSC for the first time [170]. Although the orthorhombic phase of Nb_2O_5 is formed at very high temperature (>600-700 °C), the authors synthesized a highly ordered mesoporous orthorhombic Nb_2O_5 with-

out disruption of the mesoporous structure through a well-defined synthesis strategy. In addition, m-Nb_2O_5-C was synthesized without adding a carbon source because PS segments of BCP *in-situ* converted to carbon lining the mesopores of m-Nb_2O_5-C during the heat treatment under inert atmosphere. The resulting m-Nb_2O_5-C has 30 nm pores and 76 m^2 g^{-1} surface area. It showed high reversible capacity (~190 mAh g^{-1} at current of 10 mA g^{-1} and operating voltage of 1.1-3.0 V *vs.* Li/Li^+) and excellent rate performance (~120 mAh g^{-1} at current of 5 A g^{-1}, Fig. 9(d)) with long-term cycle life for 4,000 cycles. The authors also revealed the charge storage mechanism of m-Nb_2O_5-C by defining the value of b through a cyclic voltammetry (CV) test using the Randles-Sevcik equation ($i=av^b$, a and b are variables, i is the current, v is the scan rate). The surface-controlled (b=1) and the diffusion-controlled (b=0.5) contributions of the charge storage mechanism can be separated from the equation. In agreement with Dunn's report, m-Nb_2O_5-C is not kinetically limited by solid-state diffusion, as confirmed by its *b*-value close to 1 (Fig. 9(e)) [177]. The energy (~74 Wh kg^{-1}) and power (~18,510 W kg^{-1}) of Li-HSC using m-Nb_2O_5-C anode with activated carbon cathode were much higher than the other Li-HSCs using Ti-based anodes and conventional SCs. In addition, Lee and coworkers recently reported a pH-assisted synthesis method that allows for easy control of the crystal structure of Nb_2O_5. They also revealed the optimal synthesis conditions for obtaining an orthorhombic phase, as well as the effect of the Nb_2O_5 crystal structure on the electrochemical performance [182]. Since the Lee group's paper, many researchers have focused on developing porous Nb_2O_5 anodes and various nano-Nb_2O_5 anodes for Li-HSC [183,184]. The Nb_2O_5 electrode is also attracting attention as a sodium-ion hybrid supercapacitor (Na-HSC) and a sodium-ion battery anode, demonstrating excellent electrochemical performance [40,185]. In addition to the intrinsic pseudocapacitive material (Nb_2O_5), an extrinsic pseudocapacitive material has been used for Li-HSC anode [179,186]. The battery-type electrodes can be nano-engineered to have pseudocapacitive charge storage properties through the rational design of the electrode materials such as size control, heteroatom doping, and anion intercalation. For example, a representative battery-type electrode (MoO_3) exhibited unique pseudocapacitive Li^+ storage behavior when designed in the form of an ordered mesoporous film with iso-oriented nanocrystalline walls [187]. This implies that nano-engineering could open up the new opportunities to use a wide variety of materials as anodes for Li-HSC.

More recently, a variety of conversion- and alloying-reaction based anodes have been used in Li-HSC because of their higher theoretical capacity (>500 mAh g^{-1}) compared to intercalation based anodes [188-191]. However, the conversion- and alloying-type anodes are usually not suitable for Li-HSC applications due to their poor kinetics and cycling properties. In addition, their charge storage capacities are too large to make energy balance with low capacity Li-HSC cathodes such as AC (~60 mAh g^{-1} in operating voltage range of 3.0-4.5 V *vs.* Li/Li^+). Therefore, it is quite difficult to optimize the Li-HSC full-cell operating voltage. Lim and coworkers suggested that Li_3VO_4 could be promising candidate for Li-HSC anode because of the following electrochemical properties [160]: Li_3VO_4 reacts with Li^+ through an intercalation reaction, giving a theoretical capacity of ~395 mAh g^{-1} in the operating voltage range of 0.2-1.0 V (*vs.* Li/Li^+). This indicates that Li-HSC with Li_3VO_4 anode provides much higher energy than LTO and Nb_2O_5. However, big challenges on Li_3VO_4 still remain for Li-HSC application. The electrical conductivity is low compared to the ionic conductivity, which can lead to large resistance polarization [192]. It is also important to reduce the particle size to alleviate structural stress during cycling [193]. To address these issues, the Qian group reported hierarchical porous Li_3VO_4/C nanocomposites (hp-LVO/C) synthesized by solvothermal reaction (Fig. 9(f)) [171]. Compared with the mesoporous Li_3VO_4 (mp-LVO/C), the hp-LVO/C showed improved rate capability and specific capacity mainly due to the synergistic effect of mesopores and macropores. For example, the specific capacity of hp-LVO/C was ~351 mAh g^{-1} at current of 0.1 A g^{-1} with high rate capacity of ~304 mAh g^{-1} at 2.0 A g^{-1} at an operating voltage of 0.02-3.0 V (*vs.* Li/Li^+), which is much higher than mp-LVO/C (~300 mAh g^{-1} at current of 0.1 A g^{-1} and ~200 mAh g^{-1} at current of 2.0 A g^{-1}). As can be seen in Fig. 9(g), the charge storage mechanism of hp-LVO/C is highly dependent on the surface-controlled reaction, mainly because of the hierarchical porosity and the carbon composite structure. In addition, the authors prepared hp-LVO/C-based Li-HSC using CMK-3 cathode (a representative mesoporous carbon synthesized by the hard template method). The reported Ragone plot showed that the prepared Li-HSC exhibited better energy (~105 Wh kg^{-1}) and power (~9.3 kW kg^{-1}) compared to previous results based on various metal oxide anodes (Fig. 9(h)). As another example, the Lee group investigated the internal resistance and the *b*-value trend of Li_3VO_4 during cycling with or without carbon [160]. Definitely, with a carbon shell, Li_3VO_4 resulted in an improved surface-controlled response (*b*-value close to 1) and a reduced internal resistance. In addition, the authors precisely controlled the operating voltage of Li_3VO_4-based Li-HSCs through a pre-lithiation process, resulting in much improved energy (~190 Wh kg^{-1}) and power (~18.5 kW kg^{-1}) capabilities in the operating voltage range of 0.0-4.3 V. In addition to Nb_2O_5 and Li_3VO_4, the development of new anode materials and their integration to full-cell configuration is highly necessary to significantly improve the electrochemical performance of Li-HSCs.

3. Carbonaceous Materials

In the early study of Li-HSC, graphite was recognized as one of the most promising Li-HSC anode materials because of high theoretical capacity (~372 mAh g^{-1} in the operating voltage range below 0.1 V *vs.* Li/Li^+) [196]. Indeed, graphite-based Li-HSC delivers higher energy compared to LTO-based Li-HSC due to its higher capacity and wider operating voltage range. For example, Béguin et al. reported that a high energy Li-HSC was designed using commercially available graphite and AC as the anode and cathode, respectively [194]. After carefully balancing the mass loading between the two electrodes with the Li-HSC full-cell operating voltage, the gravimetric and volumetric energy density of the graphite-based Li-HSC was estimated to be ~104 Wh kg^{-1} and ~112 Wh L^{-1} in the operating voltage range of 1.5-4.5 V, respectively. Especially when the cut-off voltage was increased to 5.0 V, the maximum energy of graphite-based Li-HSC was estimated to be ~145.8 Wh kg^{-1} (Fig. 10(a)). However, the Li^+ intercalation/de-intercalation kinetics of graphite are slower than that of LTO, Nb_2O_5, etc. This means that graphite-based Li-HSC may not be able to achieve high rate per-

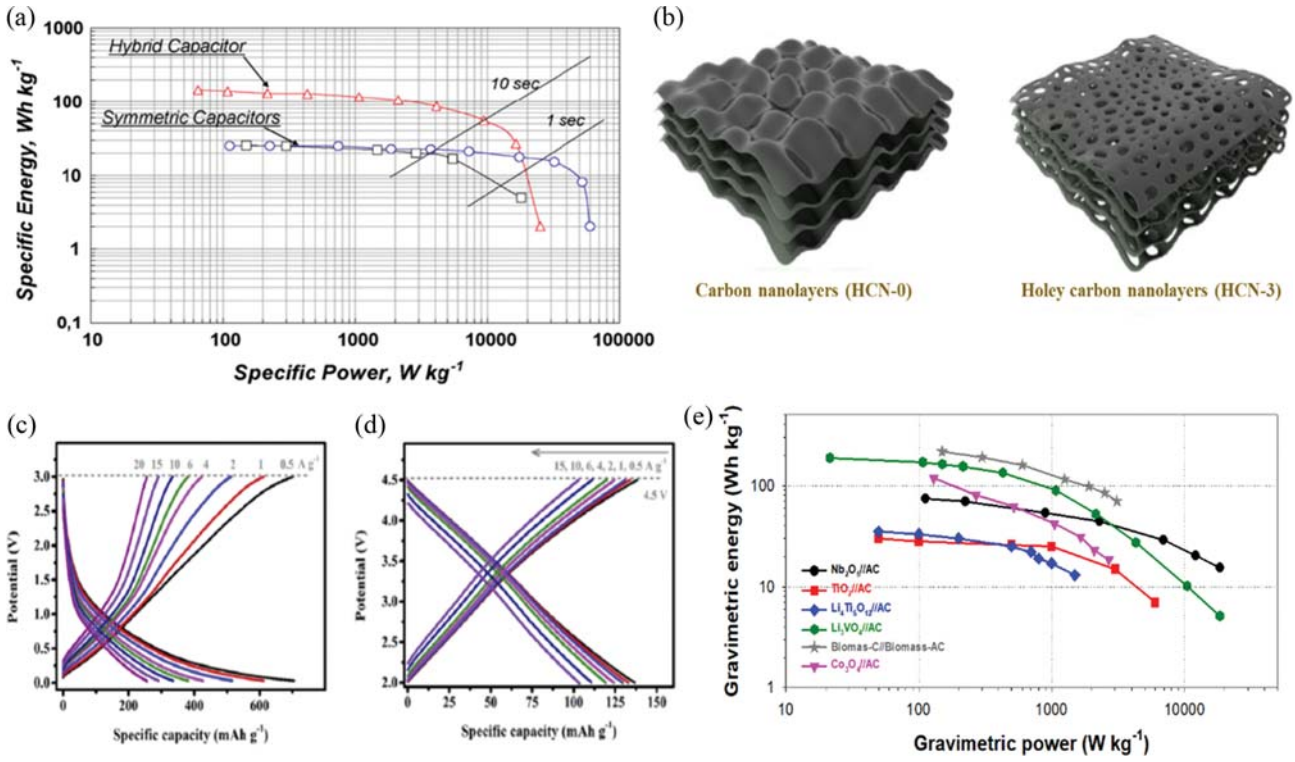

Fig. 10. (a) Ragone plot for Li-HSC using 1 M $LiPF_6$ in EC/DMC (△, red), conventional SCs using 1 M $LiPF_6$ in EC/DMC (□, black) and 1 M Et_4NBF in AN (○, blue) (Reprinted with permission from Ref. [194], Copyright 2008 Elsevier), (b) schematic illustration on HCN-0 and HCN-3, (c)-(d) specific capacity of HCN-0 and HCN-3 with increasing currents (Reprinted with permission from. Ref. [195], Copyright 2018 Elsevier), and (e) Ragone plot for Li-HSC using representative anodes.

formance, which is the main advantage of Li-HSC system. Moreover, the low Li^+ intercalation/de-intercalation voltage of graphite can lead to safety concerns as Li deposition occurs at around 0 V (*vs.* Li/Li^+) [197]. Thus, precise control of the operating voltage of graphite-based Li-HSC is highly required for long-term cycling.

The Hyeon group reported the possibility of using a mesoporous carbon material synthesized by a hard template method as an SC electrode [198,199]. Inspired by this contribution, mesoporous carbon materials have been extensively investigated as one of the promising electrode materials for various energy storage applications. In particular, precise control over the properties of carbonaceous materials (*e.g.*, surface area and functionality, pore characteristics) and carrier concentration is very important to improve electrochemical performance [200-203]. In recent years, biomass-derived porous carbons have attracted great attention as efficient and low-cost electrode materials of Li-HSC [204-209]. Ma et al. designed holey carbon nanolayers (HCNs) with targeted porosity and tailor-made morphology through multi-step synthesis and utilized them as both anode and cathode of Li-HSCs [195]. HCN-0 with a high specific surface area of 936 $m^2\ g^{-1}$ (without KOH activation, Fig. 10(b)-(c)) exhibits a reversible specific capacity of ~700 mAh g^{-1} at current of 0.5 A g^{-1} and rapid charge/discharge rate (~280 mAh g^{-1} at current of 20 A g^{-1}) in an operating voltage of 0.3-3.0 V (*vs.* Li/Li^+). Interestingly, HCN-3 (Fig. 10(b), (d)) treated by KOH activation was also used as a cathode material, resulting in a specific capacity of ~140 mAh g^{-1} at current of 0.5 A g^{-1} in the operating voltage range from 2.0 to 4.5 V (*vs.* Li/Li^+). Due to the stable cycle performance of both electrodes, Li-HSC using HCN anode and cathode showed outstanding cycle stability over 5,000 cycles with high energy (~180 Wh kg^{-1}) and power (~65 kW kg^{-1}) in the operating potential of 2.0-4.5 V. Finally, to summarize and compare the electrochemical performance of Li-HSC systems using metal oxide and carbonaceous electrodes, Ragone plots of representative results are provided (Fig. 10(e)) [160,165,169,170,191,204]. For commercialization of Li-HSC, in addition to aspects on development and design of new electrode materials, researchers should focus on a number of important factors such as pre-lithiation process, electrode thickness (mass loading), full-cell balance between anode and cathode, and full-cell operating potential.

The utilization of mesoporous carbon in Li-HSC is rare compared to that of mesoporous metal oxide. However, in recent years, amorphous mesoporous carbon has been more widely used in sodium- and potassium-ion hybrid supercapacitors (Na- and K-HSCs) than metal oxides and conventional graphite [206,210]. This is because amorphous mesoporous carbon materials offer much higher specific capacity and better rate capability than metal oxides, and Na^+ and K^+ storage mechanisms in amorphous carbon are less complicated than those in graphite [211-213]. Therefore, extensive research on the use of mesoporous carbon as an HSC electrode is still open to many researchers.

CONCLUSION AND FUTURE PERSPECTIVE

Considerable progress has been made in the field of mesoporous

materials. A wide variety of them with controllable pore size, pore structures, particle morphology, and chemical composition are now available in the literature. Mesoporous materials have been actively applied in energy storage applications due to their nanoparticle-like properties, high surface area, and large pore volume. It thus enables active materials to achieve better capacity, rapid charge/discharge performance, and stable cycle life. However, there are still many challenges and limitations in mesoporous material synthesis and energy device applications.

The main challenges for the commercialization of mesoporous materials are high production cost and difficulty of mass production. Most synthesis routes rely on either complicated multi-step procedures or the use of cost-intensive precursors. Thus, the development of a facile and scalable synthesis method is of great importance. The use of inexpensive and abundant resources such as industrial byproducts and biomass would be a promising solution [214,215]. To increase the feasibility of industrial production, it is also necessary to conduct a systematic economic analysis of the manufacture of mesoporous materials.

In addition, precise structural and morphological control over multiple length scales is an important future goal of the mesoporous materials society. Enhanced physical designability of mesoporous materials will provide new opportunities to improve material performance without altering the chemical composition. To translate the enhanced performance from the laboratory to real-industrial applications, systematic studies on the structure (morphology)-property relations in target applications are greatly required. This will provide platforms to understand fundamental electrochemical reactions at nanometer scale for various electrochemical energy storage systems.

Low electrode density and side reaction issues should be addressed for broad and commercial use of mesoporous materials in the LIB and Li-HSC market. Especially, mesoporous conversion or alloying materials, which react with Li^+ under 1.0 V (*vs.* Li/Li^+), have exhibited poor initial Coulombic efficiency (ICE) values because of their poor reversibility and electrolyte decomposition at the large surface of active materials. Considering that commercial anodes have an ICE value of more than 90%, the low efficiency at initial cycle is a serious problem for full cell design. The low density problems can be alleviated by i) controlling morphology into regular sized spheres, ii) filling pores with high capacity/density materials, and iii) balancing the porosity and the packing density in an optimal manner. To increase ICEs, iv) coating with rigid and low surface area materials on outermost surface of mesoporous composite materials can minimize side reaction by lowering electrolyte decomposition reactions. Assembling primary nanoparticles into secondary mesoporous particles has shown potential as a possible solution to alleviate the side reaction problem [216]. v) Besides, along with structure engineering, electrolyte additives for stable SEI formation and filling pores with solid-state electrolyte can be considered to design stable mesoporous materials-based electrodes. Additionally, it will also continue to find new candidates with well-designed mesoporous structure and will be able to broaden the field of energy storage research. Further researches on mesoporous active material design will not only optimize the LIB and Li-HSC performances but also find meaningful information to design next-generation energy storage systems including Li-S, Li-O_2, multivalent ion batteries, Na-HSC, and K-HSC.

ACKNOWLEDGEMENTS

J.H. acknowledges the support of the National Research Foundation of Korea (NRF) grant funded by the Korea government (MSIT) (No. 2020R1F1A1065283). E.L. thanks the support of the KRICT projects (No. SI2011-30 and SI2061-313) from the Korea Research Institute of Chemical Technology (KRICT). C.J. acknowledges the support of the NRF grant funded by the Korea government (No. 2020R1G1A1101146).

REFERENCES

1. S. Ghosh, S. M. Jeong and S. R. Polaki, *Korean J. Chem. Eng.*, **35**, 1389 (2018).
2. H. Jun, S. Kim and J. Lee, *Korean J. Chem. Eng.*, **37**, 1317 (2020).
3. N. Nitta, F. Wu, J. T. Lee and G. Yushin, *Mater. Today*, **18**, 252 (2015).
4. X. Zhang, L. Li, E. Fan, Q. Xue, Y. Bian, F. Wu and R. Chen, *Chem. Soc. Rev.*, **47**, 7239 (2018).
5. J.-M. Tarascon and M. Armand, *Nature*, **414**, 359 (2001).
6. M. Li, J. Lu, Z. Chen and K. Amine, *Adv. Mater.*, **30**, 1800561 (2018).
7. Z. W. Seh, Y. Sun, Q. Zhang and Y. Cui, *Chem. Soc. Rev.*, **45**, 5605 (2016).
8. Y. Wang, Y. Song and Y. Xia, *Chem. Soc. Rev.*, **45**, 5925 (2016).
9. C. Jiang, E. Hosono and H. Zhou, *Nano Today*, **1**, 28 (2006).
10. K. T. Lee and J. Cho, *Nano Today*, **6**, 28 (2011).
11. Y. Sun, N. Liu and Y. Cui, *Nat. Energy*, **1**, 16071 (2016).
12. E. Lim, C. Jo and J. Lee, *Nanoscale*, **8**, 7827 (2016).
13. Y. Ye, C. Jo, I. Jeong and J. Lee, *Nanoscale*, **5**, 4584 (2013).
14. W. Li, J. Liu and D. Zhao, *Nat. Rev. Mater.*, **1**, 16023 (2016).
15. Y. Wang, H. Guo, X. Luo, X. Liu, Z. Hu, L. Han and Z. Zhang, *Small*, **15**, 1805277 (2019).
16. C. Li, Q. Li, Y.V. Kaneti, D. Hou, Y. Yamauchi and Y. Mai, *Chem. Soc. Rev.*, **49**, 4681 (2020).
17. Z. Liu, X. Yuan, S. Zhang, J. Wang, Q. Huang, N. Yu, Y. Zhu, L. Fu, F. Wang, Y. Chen and Y. Wu, *NPG Asia Mater.*, **11**, 12 (2019).
18. F. Wang, Z. Chang, X. Wang, Y. Wang, B. Chen, Y. Zhu and Y. Wu, *J. Mater. Chem. A*, **3**, 4840 (2015).
19. W.-G. Lim, S. Kim, C. Jo and J. Lee, *Angew. Chem., Int. Ed.*, **58**, 18746 (2019).
20. E. V. Sturm and H. Cölfen, *Chem. Soc. Rev.*, **45**, 5821 (2016).
21. O. M. Yaghi, M. O'keeffe, N. W. Ockwig, H. K. Chae, M. Eddaoudi and J. Kim, *Nature*, **423**, 705 (2003).
22. W. Xuan, C. Zhu, Y. Liu and Y. Cui, *Chem. Soc. Rev.*, **41**, 1677 (2012).
23. J. Hwang, A. Ejsmont, R. Freund, J. Goscianska, B. V. K. J. Schmidt and S. Wuttke, *Chem. Soc. Rev.*, **49**, 3348 (2020).
24. J. Hwang, R. Walczak, M. Oschatz, N. V. Tarakina and B. V. K. J. Schmidt, *Small*, **15**, 1901986 (2019).
25. J. Hwang, T. Heil, M. Antonietti and B. V. K. J. Schmidt, *J. Am. Chem. Soc.*, **140**, 2947 (2018).
26. X. Zhang, A. Chen, M. Zhong, Z. Zhang, X. Zhang, Z. Zhou and

X.-H. Bu, *Electrochem. Energy Rev.*, **2**, 29 (2019).
27. J. Hwang, R. Yan, M. Oschatz and B. V. K. J. Schmidt, *J. Mater. Chem. A*, **6**, 23521 (2018).
28. C. Kresge, M. Leonowicz, W. J. Roth, J. Vartuli and J. Beck, *Nature*, **359**, 710 (1992).
29. D. Zhao, J. Feng, Q. Huo, N. Melosh, G. H. Fredrickson, B. F. Chmelka and G. D. Stucky, *Science*, **279**, 548 (1998).
30. M. Templin, A. Franck, A. Du Chesne, H. Leist, Y. Zhang, R. Ulrich, V. Schädler and U. Wiesner, *Science*, **278**, 1795 (1997).
31. P. Yang, D. Zhao, D. I. Margolese, B. F. Chmelka and G. D. Stucky, *Nature*, **396**, 152 (1998).
32. J. Lee, M. C. Orilall, S. C. Warren, M. Kamperman, F. J. DiSalvo and U. Wiesner, *Nat. Mater.*, **7**, 222 (2008).
33. Y. Zou, X. Zhou, Y. Zhu, X. Cheng, D. Zhao and Y. Deng, *Acc. Chem. Res.*, **52**, 714 (2019).
34. T. N. Hoheisel, K. Hur and U. B. Wiesner, *Prog. Polym. Sci.*, **40**, 3 (2015).
35. Y. Zhu, Y. Zhao, J. Ma, X. Cheng, J. Xie, P. Xu, H. Liu, H. Liu, H. Zhang, M. Wu, A. A. Elzatahry, A. Alghamdi, Y. Deng and D. Zhao, *J. Am. Chem. Soc.*, **139**, 10365 (2017).
36. J. Hwang, S. H. Woo, J. Shim, C. Jo, K. T. Lee and J. Lee, *ACS Nano*, **7**, 1036 (2013).
37. M. Niederberger, *Acc. Chem. Res.*, **40**, 793 (2007).
38. B. Tian, X. Liu, B. Tu, C. Yu, J. Fan, L. Wang, S. Xie, G. D. Stucky and D. Zhao, *Nat. Mater.*, **2**, 159 (2003).
39. J. Hwang, J. Kim, E. Ramasamy, W. Choi and J. Lee, *Micropor. Mesopor. Mater.*, **143**, 149 (2011).
40. H. Kim, E. Lim, C. Jo, G. Yoon, J. Hwang, S. Jeong, J. Lee and K. Kang, *Nano Energy*, **16**, 62 (2015).
41. C. Jo, Y. Kim, J. Hwang, J. Shim, J. Chun and J. Lee, *Chem. Mater.*, **26**, 3508 (2014).
42. J. Hwang, C. Jo, K. Hur, J. Lim, S. Kim and J. Lee, *J. Am. Chem. Soc.*, **136**, 16066 (2014).
43. C. Jo, J. Hwang, H. Song, A. H. Dao, Y.-T. Kim, S. H. Lee, S. W. Hong, S. Yoon and J. Lee, *Adv. Funct. Mater.*, **23**, 3747 (2013).
44. J. Zhang, Y. Deng, D. Gu, S. Wang, L. She, R. Che, Z. S. Wang, B. Tu, S. Xie and D. Zhao, *Adv. Energy Mater.*, **1**, 241 (2011).
45. X. Xiao, L. Liu, J. Ma, Y. Ren, X. Cheng, Y. Zhu, D. Zhao, A. A. Elzatahry, A. Alghamdi and Y. Deng, *ACS Appl. Mater. Interfaces*, **10**, 1871 (2018).
46. X. Zhou, Y. Zhu, W. Luo, Y. Ren, P. Xu, A. A. Elzatahry, X. Cheng, A. Alghamdi, Y. Deng and D. Zhao, *J. Mater. Chem. A*, **4**, 15064 (2016).
47. J. Hwang, C. Jo, M. G. Kim, J. Chun, E. Lim, S. Kim, S. Jeong, Y. Kim and J. Lee, *ACS Nano*, **9**, 5299 (2015).
48. C. Jo, W.-G. Lim, A. H. Dao, S. Kim, S. Kim, S. Yoon and J. Lee, *J. Mater. Chem. A*, **5**, 24782 (2017).
49. Z. Wang, Y. Zhu, W. Luo, Y. Ren, X. Cheng, P. Xu, X. Li, Y. Deng and D. Zhao, *Chem. Mater.*, **28**, 7773 (2016).
50. S. Kim, C. Choi, J. Hwang, J. Park, J. Jeong, H. Jun, S. Lee, S.-K. Kim, J. H. Jang, Y. Jung and J. Lee, *ACS Nano*, **14**, 4988 (2020).
51. C. Yi, Y. Yang, B. Liu, J. He and Z. Nie, *Chem. Soc. Rev.*, **49**, 465 (2020).
52. R. Buonsanti, T. E. Pick, N. Krins, T. J. Richardson, B. A. Helms and D. J. Milliron, *Nano Lett.*, **12**, 3872 (2012).
53. M. C. Orilall, F. Matsumoto, Q. Zhou, H. Sai, H. D. Abruña, F. J. DiSalvo and U. Wiesner, *J. Am. Chem. Soc.*, **131**, 9389 (2009).
54. E. Kang, H. Jung, J.-G. Park, S. Kwon, J. Shim, H. Sai, U. Wiesner, J. K. Kim and J. Lee, *ACS Nano*, **5**, 1018 (2011).
55. J. Hwang, G. Kwak, Y.-J. Lee, Y. T. Kim, I. Jeong, S. Kim, K.-W. Jun, K.-S. Ha and J. Lee, *J. Mater. Chem. A*, **3**, 23725 (2015).
56. J. Shim, J. Lee, Y. Ye, J. Hwang, S.-K. Kim, T.-H. Lim, U. Wiesner and J. Lee, *ACS Nano*, **6**, 6870 (2012).
57. Y. Mun, J. Shim, K. Kim, J. W. Han, S.-K. Kim, Y. Ye, J. Hwang, S. Lee, J. Jang, Y.-T. Kim and J. Lee, *RSC Adv.*, **6**, 88255 (2016).
58. S. Kim and J. Lee, *Natl. Sci. Rev.*, **7**, 1635 (2020).
59. S. Koizumi, H. Hasegawa and T. Hashimoto, *Macromolecules*, **27**, 6532 (1994).
60. K. Nakanishi and N. Tanaka, *Acc. Chem. Res.*, **40**, 863 (2007).
61. H. Sai, K. W. Tan, K. Hur, E. Asenath-Smith, R. Hovden, Y. Jiang, M. Riccio, D. A. Muller, V. Elser, L. A. Estroff, S. M. Gruner and U. Wiesner, *Science*, **341**, 530 (2013).
62. S. Kim, I. Jeong, J. Hwang, M. J. Ko and J. Lee, *Chem. Commun.*, **53**, 4100 (2017).
63. C. Jo, J. Hwang, W.-G. Lim, J. Lim, K. Hur and J. Lee, *Adv. Mater.*, **30**, 1703829 (2018).
64. J. Kim, C. Jo, W.-G. Lim, S. Jung, Y. M. Lee, J. Lim, H. Lee, J. Lee and W. J. Kim, *Adv. Mater.*, **30**, 1707557 (2018).
65. J. Hwang, S. Kim, U. Wiesner and J. Lee, *Adv. Mater.*, **30**, 1801127 (2018).
66. Y. Zhou, M. Ghaffari, M. Lin, E. M. Parsons, Y. Liu, B. L. Wardle and Q. Zhang, *Electrochim. Acta*, **111**, 608 (2013).
67. S. Kim, J. Hwang, J. Lee and J. Lee, *Sci. Adv.*, **6**, eabb3814 (2020).
68. S. Kim, M. Ju, J. Lee, J. Hwang and J. Lee, *J. Am. Chem. Soc.*, **142**, 9250 (2020).
69. S. Hobbs, M. Dekkers and V. Watkins, *Polymer*, **29**, 1598 (1988).
70. R. Schmuch, R. Wagner, G. Hörpel, T. Placke and M. Winter, *Nat. Energy*, **3**, 267 (2018).
71. J.-T. Han, Y.-H. Huang and J. B. Goodenough, *Chem. Mater.*, **23**, 2027 (2011).
72. H. Liu, W. Li, D. Shen, D. Zhao and G. Wang, *J. Am. Chem. Soc.*, **137**, 13161 (2015).
73. H. Liu, Z. Bi, X.-G. Sun, R. R. Unocic, M. P. Paranthaman, S. Dai and G. M. Brown, *Adv. Mater.*, **23**, 3450 (2011).
74. E. Kang, Y. S. Jung, G.-H. Kim, J. Chun, U. Wiesner, A. C. Dillon, J. K. Kim and J. Lee, *Adv. Funct. Mater.*, **21**, 4349 (2011).
75. M. S. Whittingham, *Chem. Rev.*, **114**, 11414 (2014).
76. R. C. Massé, C. Liu, Y. Li, L. Mai and G. Cao, *Natl. Sci. Rev.*, **4**, 26 (2016).
77. C. Jiang, M. Wei, Z. Qi, T. Kudo, I. Honma and H. Zhou, *J. Power Sources*, **166**, 239 (2007).
78. M. Wagemaker and F. M. Mulder, *Acc. Chem. Res.*, **46**, 1206 (2013).
79. V. Augustyn, P. Simon and B. Dunn, *Energy Environ. Sci.*, **7**, 1597 (2014).
80. Y. Ren, A. R. Armstrong, F. Jiao and P. G. Bruce, *J. Am. Chem. Soc.*, **132**, 996 (2010).
81. Y.-G. Guo, J.-S. Hu and L.-J. Wan, *Adv. Mater.*, **20**, 2878 (2008).
82. J.-T. Han and J. B. Goodenough, *Chem. Mater.*, **23**, 3404 (2011).
83. B. Guo, X. Yu, X.-G. Sun, M. Chi, Z.-A. Qiao, J. Liu, Y.-S. Hu, X.-Q. Yang, J. B. Goodenough and S. Dai, *Energy Environ. Sci.*, **7**, 2220 (2014).
84. Y. Yang, Y. Yue, L. Wang, X. Cheng, Y. Hu, Z.-z. Yang, R. Zhang, B. Jin and R. Sun, *Int. J. Hydrogen Energy*, **45**, 12583 (2020).

85. M. Liu, H. Dong, S. Zhang, X. Chen, Y. Sun, S. Gao, J. Xu, X. Wu, A. Yuan and W. Lu, *ChemElectroChem*, **6**, 3959 (2019).
86. G. Liu, L. Zhao, R. Sun, W. Chen, M. Hu, M. Liu, X. Duan and T. Zhang, *Electrochim. Acta*, **259**, 20 (2018).
87. H. Li, L. Shen, G. Pang, S. Fang, H. Luo, K. Yang and X. Zhang, *Nanoscale*, **7**, 619 (2015).
88. M. Madian, A. Eychmüller and L. Giebeler, *Batteries*, **4**, 7 (2018).
89. X. Yan, Z. Wang, M. He, Z. Hou, T. Xia, G. Liu and X. Chen, *Energy Tech.*, **3**, 801 (2015).
90. H.-G. Jung, C. S. Yoon, J. Prakash and Y.-K. Sun, *J. Phy. Chem. C*, **113**, 21258 (2009).
91. Y.-G. Guo, Y.-S. Hu and J. Maier, *Chem. Commun.*, **26**, 2783 (2006).
92. L. Yu, H. B. Wu and X. W. Lou, *Adv. Mater.*, **25**, 2296 (2013).
93. J. Haetge, P. Hartmann, K. Brezesinski, J. Janek and T. Brezesinski, *Chem. Mater.*, **23**, 4384 (2011).
94. A. Nugroho, K. Y. Chung and J. Kim, *J. Phy. Chem. C*, **118**, 183 (2014).
95. Y. Yoo and Y. C. Kang, *J. Alloys Compd.*, **776**, 722 (2019).
96. J. Y. Cheong, J.-W. Jung, D.-Y. Youn, C. Kim, S. Yu, S.-H. Cho, K. R. Yoon and I.-D. Kim, *J. Power Sources*, **360**, 434 (2017).
97. G. Ma, K. Li, Y. Li, B. Gao, T. Ding, Q. Zhong, J. Su, L. Gong, J. Chen, L. Yuan, B. Hu, J. Zhou and K. Huo, *ChemElectroChem*, **3**, 1360 (2016).
98. J. B. Cook, H.-S. Kim, Y. Yan, J. S. Ko, S. Robbennolt, B. Dunn and S. H. Tolbert, *Adv. Energy Mater.*, **6**, 1501937 (2016).
99. S. Chen, Z. Chen and C. Cao, *Electrochim. Acta*, **199**, 51 (2016).
100. J.-y. Luo, Y.-g. Wang, H.-m. Xiong and Y.-y. Xia, *Chem. Mater.*, **19**, 4791 (2007).
101. B. K. Lesel, J. S. Ko, B. Dunn and S. H. Tolbert, *ACS Nano*, **10**, 7572 (2016).
102. J. Qian, M. Zhou, Y. Cao, X. Ai and H. Yang, *J. Phys. Chem. C*, **114**, 3477 (2010).
103. G. Wang, H. Liu, J. Liu, S. Qiao, G. M. Lu, P. Munroe and H. Ahn, *Adv. Mater.*, **22**, 4944 (2010).
104. D. Saikia, J. R. Deka, C.-J. Chou, C.-H. Lin, Y.-C. Yang and H.-M. Kao, *ACS Appl. Energy Mater.*, **2**, 1121 (2019).
105. F. Jiao, K. M. Shaju and P. G. Bruce, *Angew. Chem., Int. Ed.*, **44**, 6550 (2005).
106. J. Li, S. Xiong, Y. Liu, Z. Ju and Y. Qian, *ACS Appl. Mater. Interfaces*, **5**, 981 (2013).
107. J. K. Shon, H. S. Lee, G. O. Park, J. Yoon, E. Park, G. S. Park, S. S. Kong, M. Jin, J.-M. Choi, H. Chang, S. Doo, J. M. Kim, W.-S. Yoon, C. Pak, H. Kim and G. D. Stucky, *Nat. Commun.*, **7**, 11049 (2016).
108. Y. Chen, B. Song, M. Li, L. Lu and J. Xue, *Adv. Funct. Mater.*, **24**, 319 (2014)
109. J. Chun, C. Jo, S. Sahgong, M. G. Kim, E. Lim, D. H. Kim, J. Hwang, E. Kang, K. A. Ryu, Y. S. Jung, Y. Kim and J. Lee, *ACS Appl. Mater. Interfaces*, **8**, 35180 (2016).
110. W.-G. Lim, Y. Mun, A. Cho, C. Jo, S. Lee, J. W. Han and J. Lee, *ACS Nano*, **12**, 6013 (2018).
111. J. Song, T. Xu, M. L. Gordin, P. Zhu, D. Lv, Y.-B. Jiang, Y. Chen, Y. Duan and D. Wang, *Adv. Funct. Mater.*, **24**, 1243 (2014).
112. S.-H. Yu, S. H. Lee, D. J. Lee, Y.-E. Sung and T. Hyeon, *Small*, **12**, 2146 (2016).
113. K. Cao, T. Jin, L. Yang and L. Jiao, *Mater. Chem. Front.*, **1**, 2213 (2017).
114. M. D. Bhatt and J. Y. Lee, *Int. J. Hydrogen Energy*, **44**, 10852 (2019).
115. K. Zhang, S. Liang, X. Yin, P. Gao, R. Ding and E. Liu, *J. Solid State Chem.*, **286**, 121300 (2020).
116. B. Qu, M. Zhang, D. Lei, Y. Zeng, Y. Chen, L. Chen, Q. Li, Y. Wang and T. Wang, *Nanoscale*, **3**, 3646 (2011).
117. H. Liu, D. Su, G. Wang and S. Z. Qiao, *J. Mater. Chem.*, **22**, 17437 (2012).
118. S. Yoon, C. Jo, S. Y. Noh, C. W. Lee, J. H. Song and J. Lee, *Phys. Chem. Chem. Phys.*, **13**, 11060 (2011).
119. H. Liu, G. Wang, J. Liu, S. Qiao and H. Ahn, *J. Mater. Chem.*, **21**, 3046 (2011).
120. S. Sun, Z. Wen, J. Jin, Y. Cui and Y. Lu, *Micropor. Mesopor. Mater.*, **169**, 242 (2013).
121. G. O. Park, J. Yoon, S. B. Park, Z. Li, Y. S. Choi, W.-S. Yoon, H. Kim and J. M. Kim, *Small*, **14**, 1702985 (2018).
122. J. Lee, J. Kim and T. Hyeon, *Adv. Mater.*, **18**, 2073 (2006).
123. E. Kang, Y. S. Jung, A. S. Cavanagh, G.-H. Kim, S. M. George, A. C. Dillon, J. K. Kim and J. Lee, *Ad. Funct. Mater.*, **21**, 2430 (2011).
124. B. Zhu, G. Guo, G. Wu, Y. Zhang, A. Dong, J. Hu and D. Yang, *J. Alloys Compd.*, **775**, 776 (2019).
125. J. Chun, C. Jo, E. Lim, K. C. Roh and J. Lee, *Mater. Lett.*, **207**, 89 (2017).
126. J. Hwang and J. Chun, *J. Am. Ceram. Soc.*, **102**, 6475 (2019).
127. X. Ji, K. T. Lee and L. F. Nazar, *Nat. Mater.*, **8**, 500 (2009).
128. A. Manthiram, Y. Fu, S.-H. Chung, C. Zu and Y.-S. Su, *Chem. Rev.*, **114**, 11751 (2014).
129. L. Zhang, Y. Wang, Z. Niu and J. Chen, *Carbon*, **141**, 400 (2019).
130. W.-G. Lim, C. Jo, J. Lee and D. S. Hwang, *Korean J. Chem. Eng.*, **35**, 579 (2018).
131. M. Oschatz, J. T. Lee, H. Kim, W. Nickel, L. Borchardt, W. I. Cho, C. Ziegler, S. Kaskel and G. Yushin, *J. Mater. Chem. A*, **2**, 17649 (2014).
132. W.-G. Lim, C. Jo, A. Cho, J. Hwang, S. Kim, J. W. Han and J. Lee, *Adv. Mater.*, **31**, 1806547 (2019).
133. J. T. Lee, Y. Zhao, H. Kim, W. I. Cho and G. Yushin, *J. Power Sources*, **248**, 752 (2014).
134. J. T. Lee, Y. Zhao, S. Thieme, H. Kim, M. Oschatz, L. Borchardt, A. Magasinski, W.-I. Cho, S. Kaskel and G. Yushin, *Adv. Mater.*, **25**, 4573 (2013).
135. W. Luo, Y. Wang, L. Wang, W. Jiang, S.-L. Chou, S. X. Dou, H. K. Liu and J. Yang, *ACS Nano*, **10**, 10524 (2016).
136. R. Zhang, Y. Du, D. Li, D. Shen, J. Yang, Z. Guo, H. K. Liu, A. A. Elzatahry and D. Zhao, *Adv. Mater.*, **26**, 6749 (2014).
137. H. Kim, G. O. Park, Y. Kim, S. Muhammad, J. Yoo, M. Balasubramanian, Y.-H. Cho, M.-G. Kim, B. Lee, K. Kang, H. Kim, J. M. Kim and W.-S. Yoon, *Chem. Mater.*, **26**, 6361 (2014).
138. M. Obrovac and V. Chevrier, *Chem. Rev.*, **114**, 11444 (2014).
139. Y. Jin, B. Zhu, Z. Lu, N. Liu and J. Zhu, *Adv. Energy Mater.*, **7**, 1700715 (2017).
140. C. K. Chan, H. Peng, G. Liu, K. McIlwrath, X. F. Zhang, R. A. Huggins and Y. Cui, *Nat. Nanotech.*, **3**, 31 (2008).
141. D. Lin, Z. Lu, P.-C. Hsu, H. R. Lee, N. Liu, J. Zhao, H. Wang, C. Liu and Y. Cui, *Energy Environ. Sci.*, **8**, 2371 (2015).
142. H. Kim, M. Seo, M.-H. Park and J. Cho, *Angew. Chem., Int. Ed.*, **49**, 2146 (2010).
143. C. Jo, A. S. Groombridge, J. De La Verpilliere, J. T. Lee, Y. Son, H.-L.

Liang, A. M. Boies and M. De Volder, *ACS Nano*, **14**, 698 (2020).
144. H. Kim and J. Cho, *Nano Lett.*, **8**, 3688 (2008).
145. H. Jia, P. Gao, J. Yang, J. Wang, Y. Nuli and Z. Yang, *Adv. Energy Mater.*, **1**, 1036 (2011).
146. J. Chun, S. An and J. Lee, *J. Mater. Chem. A*, **3**, 21899 (2015).
147. J. Chen, L. Yang, S. Fang and S.-i. Hirano, Electro*Chem. Commun.*, **13**, 848 (2011).
148. D. H. Youn, A. Heller and C. B. Mullins, *Chem. Mater.*, **28**, 1343 (2016).
149. M. Zhao, D.-L. Zhao, X.-Y. Han, H.-X. Yang, Y.-J. Duan and X.-M. Tian, *Electrochim. Acta*, **287**, 21 (2018).
150. S. Choi, Y.-G. Cho, J. Kim, N.-S. Choi, H.-K. Song, G. Wang and S. Park, *Small*, **13**, 1603045 (2017).
151. D. H. Youn, N. A. Patterson, H. Park, A. Heller and C. B. Mullins, *ACS Appl. Mater. Interfaces*, **8**, 27788 (2016).
152. D. Bresser, S. Passerini and B. Scrosati, *Energy Environ. Sci.*, **9**, 3348 (2016).
153. H. Kim, D.-S. Yang, J. H. Um, M. Balasubramanian, J. Yoo, H. Kim, S. B. Park, J. M. Kim and W.-S. Yoon, *J. Power Sources*, **413**, 241 (2019).
154. K. H. Seng, M.-h. Park, Z. P. Guo, H. K. Liu and J. Cho, *Nano Lett.*, **13**, 1230 (2013).
155. C. Marino, L. Boulet, P. Gaveau, B. Fraisse and L. Monconduit, *J. Mater. Chem.*, **22**, 22713 (2012).
156. Y. Xia, S. Han, Y. Zhu, Y. Liang and M. Gu, *Energy Storage Mater.*, **18**, 125 (2019).
157. J. Lin, J.-M. Lim, D. H. Youn, K. Kawashima, J.-H. Kim, Y. Liu, H. Guo, G. Henkelman, A. Heller and C. B. Mullins, *ACS Nano*, **11**, 10347 (2017).
158. S. Dong, C. Li, Z. Li, L. Zhang and L. Yin, *Small*, **14**, 1704517 (2018).
159. K. Jost, G. Dion and Y. Gogotsi, *J. Mater. Chem. A*, **2**, 10776 (2014).
160. E. Lim, W.-G. Lim, C. Jo, J. Chun, M.-H. Kim, K. C. Roh and J. Lee, *J. Mater. Chem. A*, **5**, 20969 (2017).
161. L. L. Zhang and X. Zhao, *Chem. Soc. Rev.*, **38**, 2520 (2009).
162. P. Simon, Y. Gogotsi and B. Dunn, *Science*, **343**, 1210 (2014).
163. G. G. Amatucci, F. Badway, A. Du Pasquier and T. Zheng, *J. Electrochem. Soc.*, **148**, A930 (2001).
164. K. Naoi, S. Ishimoto, J.-i. Miyamoto and W. Naoi, *Energy Environ. Sci.*, **5**, 9363 (2012).
165. H. Kim, M.-Y. Cho, M.-H. Kim, K.-Y. Park, H. Gwon, Y. Lee, K. C. Roh and K. Kang, *Adv. Energy Mater.*, **3**, 1500 (2013).
166. Y. Lee, S. Kim, J. H. Lee, K. C. Roh, E. Lim and J. Lee, *RSC Adv.*, **9**, 37882 (2019).
167. V. Aravindan, J. Gnanaraj, Y.-S. Lee and S. Madhavi, *Chem. Rev.*, **114**, 11619 (2014).
168. H. Kim, K.-Y. Park, M.-Y. Cho, M.-H. Kim, J. Hong, S.-K. Jung, K. C. Roh and K. Kang, *ChemElectroChem*, **1**, 125 (2014).
169. H.-G. Jung, N. Venugopal, B. Scrosati and Y.-K. Sun, *J. Power Sources*, **221**, 266 (2013).
170. E. Lim, H. Kim, C. Jo, J. Chun, K. Ku, S. Kim, H. I. Lee, I.-S. Nam, S. Yoon, K. Kang and J. Lee, *ACS Nano*, **8**, 8968 (2014).
171. X. Xu, F. Niu, D. Zhang, C. Chu, C. Wang, J. Yang and Y. Qian, *J. Power Sources*, **384**, 240 (2018).
172. L.-f. Que, F.-d. Yu, Z.-b. Wang and D.-m. Gu, *Electrochim. Acta*, **222**, 27 (2016).
173. K. Naoi, W. Naoi, S. Aoyagi, J.-i. Miyamoto and T. Kamino, *Acc. Chem. Res.*, **46**, 1075 (2013).
174. T. Ohzuku, A. Ueda and N. Yamamoto, *J. Electrochem. Soc.*, **142**, 1431 (1995).
175. M. Inaba, Y. Oba, F. Niina, Y. Murota, Y. Ogino, A. Tasaka and K. Hirota, *J. Power Sources*, **189**, 580 (2009).
176. K. Naoi, S. Ishimoto, Y. Isobe and S. Aoyagi, *J. Power Sources*, **195**, 6250 (2010).
177. V. Augustyn, J. Come, M. A. Lowe, J. W. Kim, P.-L. Taberna, S. H. Tolbert, H. D. Abruña, P. Simon and B. Dunn, *Nat. Mater.*, **12**, 518 (2013).
178. J. Come, V. Augustyn, J. W. Kim, P. Rozier, P.-L. Taberna, P. Gogotsi, J. W. Long, B. Dunn and P. Simon, *J. Electrochem. Soc.*, **161**, A718 (2014).
179. C. Choi, D. S. Ashby, D. M. Butts, R. H. DeBlock, Q. Wei, J. Lau and B. Dunn, *Nat. Rev. Mater.*, **5**, 5 (2020).
180. J. W. Kim, V. Augustyn and B. Dunn, *Adv. Energy Mater.*, **2**, 141 (2012).
181. A. L. Viet, M. V. Reddy, R. Jose, B. V. R. Chowdari and S. Ramakrishna, *J. Phys. Chem. C*, **114**, 664 (2010).
182. E. Lim, C. Jo, H. Kim, M.-H. Kim, Y. Mun, J. Chun, Y. Ye, J. Hwang, K.-S. Ha, K. C. Roh, K. Kang, S. Yoon and J. Lee, *ACS Nano*, **9**, 7497 (2015).
183. L. Kong, C. Zhang, S. Zhang, J. Wang, R. Cai, C. Lv, W. Qiao, L. Ling and D. Long, *J. Mater. Chem. A*, **2**, 17962 (2014).
184. S. Liu, J. Zhou, Z. Cai, G. Fang, Y. Cai, A. Pan and S. Liang, *J. Mater. Chem. A*, **4**, 17838 (2016).
185. E. Lim, C. Jo, M. S. Kim, M.-H. Kim, J. Chun, H. Kim, J. Park, K. C. Roh, K. Kang, S. Yoon and J. Lee, *Adv. Funct. Mater.*, **26**, 3711 (2016).
186. F. Yu, T. Huang, P. Zhang, Y. Tao, F.-Z. Cui, Q. Xie, S. Yao and F. Wang, *Energy Storage Mater.*, **22**, 235 (2019).
187. T. Brezesinski, J. Wang, S. H. Tolbert and B. Dunn, *Nat. Mater.*, **9**, 146 (2010).
188. R. Wang, J. Lang, P. Zhang, Z. Lin and X. Yan, *Adv. Funct. Mater.*, **25**, 2270 (2015).
189. R. Yi, S. Chen, J. Song, M. L. Gordin, A. Manivannan and D. Wang, *Adv. Funct. Mater.*, **24**, 7433 (2014).
190. F. Zhang, T. Zhang, X. Yang, L. Zhang, K. Leng, Y. Huang and Y. Chen, *Energy Environ. Sci.*, **6**, 1623 (2013).
191. P. Sennu, S. Madhavi, V. Aravindan and Y.-S. Lee, *ACS Nano*, **14**, 10648 (2020).
192. L. Shen, H. Lv, S. Chen, P. Kopold, P. A. van Aken, X. Wu, J. Maier and Y. Yu, *Adv. Mater.*, **29**, 1700142 (2017).
193. H. Li, X. Liu, T. Zhai, D. Li and H. Zhou, *Adv. Energy Mater.*, **3**, 428 (2013).
194. V. Khomenko, E. Raymundo-Piñero and F. Béguin, *J. Power Sources*, **177**, 643 (2008).
195. C. Li, X. Zhang, K. Wang, X. Sun and Y. Ma, *J. Power Sources*, **400**, 468 (2018).
196. S. R. Sivakkumar and A. G. Pandolfo, *Electrochim. Acta*, **65**, 280 (2012).
197. E. Lim, H. Shim, S. Fleischmann and V. Presser, *J. Mater. Chem. A*, **6**, 9480 (2018).
198. J. Lee, S. Yoon, T. Hyeon, S. M. Oh and K. B. Kim, *Chem. Commun.*, 2177 (1999).

199. S. Yoon, J. Lee, T. Hyeon and S. M. Oh, *J. Electrochem. Soc.*, **147**, 2507 (2000).
200. M. L. Divya, S. Natarajan, Y.-S. Lee and V. Aravindan, *ChemSusChem*, **12**, 4353 (2019).
201. D. Puthusseri, V. Aravindan, S. Madhavi and S. Ogale, *Electrochim. Acta*, **130**, 766 (2014).
202. R. Satish, A. Vanchiappan, C. L. Wong, K. W. Ng and M. Srinivasan, *Electrochim. Acta*, **182**, 474 (2015).
203. S. Chhatre, V. Aravindan, D. Puthusseri, A. Banerjee, S. Madhavi, P. P. Wadgaonkar and S. Ogale, *Mater. Today Commun.*, **4**, 166 (2015).
204. P. Sennu, N. Arun, S. Madhavi, V. Aravindan and Y.-S. Lee, *J. Power Sources*, **414**, 96 (2019).
205. P. Sennu, H.-J. Choi, S.-G. Baek, V. Aravindan and Y.-S. Lee, *Carbon*, **98**, 58 (2016).
206. S. Natarajan, Y.-S. Lee and V. Aravindan, *Chem. Asian J.*, **14**, 936 (2019).
207. M. Maharjan, M. Ulaganathan, V. Aravindan, S. Sreejith, Q. Yan, S. Madhavi, J.-Y. Wang and T. M. Lim, *ChemistrySelect*, **2**, 5051 (2017).
208. P. Sennu, V. Aravindan, M. Ganesan, Y.-G. Lee and Y.-S. Lee, *ChemSusChem*, **9**, 849 (2016).
209. A. Jain, S. Jayaraman, M. Ulaganathan, R. Balasubramanian, V. Aravindan, M. P. Srinivasan and S. Madhavi, *Electrochim. Acta*, **228**, 131 (2017).
210. S. Jayaraman, A. Jain, M. Ulaganathan, E. Edison, M. P. Srinivasan, R. Balasubramanian, V. Aravindan and S. Madhavi, *Chem. Eng. J.*, **316**, 506 (2017).
211. H. Liu, M. Jia, N. Sun, B. Cao, R. Chen, Q. Zhu, F. Wu, N. Qiao and B. Xu, *ACS Appl. Mater. Interfaces*, **7**, 27124 (2015).
212. W. Wang, J. Zhou, Z. Wang, L. Zhao, P. Li, Y. Yang, C. Yang, H. Huang and S. Guo, *Adv. Energy Mater.*, **8**, 1701648 (2018).
213. H. Kim, J. Hong, Y.-U. Park, J. Kim, I. Hwang and K. Kang, *Adv. Funct. Mater.*, **25**, 534 (2015).
214. L. Fan, P. Sun, L. Yang, Z. Xu and J. Han, *Korean J. Chem. Eng.*, **37**, 166 (2020).
215. J. Chun, Y. M. Gu, J. Hwang, K. K. Oh and J. H. Lee, *J. Ind. Eng. Chem.*, **81**, 135 (2020).
216. N. Liu, Z. Lu, J. Zhao, M. T. McDowell, H.-W. Lee, W. Zhao and Y. Cui, *Nat. Nanotech.*, **9**, 187 (2014).

Jongkook Hwang received his Ph.D. in department of chemical engineering from Pohang University of Science and Technology (POSTECH) in 2016. After his first post-doctoral training at Max Planck Institute of Colloids and Interfaces, he moved to Utrecht University where he worked on development of heterogeneous catalysts for preferential CO oxidation in H_2. In 2020, he was appointed as an assistant professor in department of chemical engineering at Ajou University, Korea. His research interest is synthesis of nanoporous materials with well-defined structures and morphologies for energy- and catalytic applications.

Changshin Jo obtained his B.S. (2010) and Ph.D. (2016) degrees in Chemical Engineering from Pohang University of Science and Technology (POSTECH). After postdoctoral research at POSTECH (with Prof. Jinwoo Lee) and University of Cambridge (as Marie Skłodowska-Curie Fellow with Prof. Michael De Volder), he joined the faculty of the School of Chemical Engineering and Materials Science at Chung-Ang University. His current research interests focus on scalable synthesis of nanostructured materials for energy storage applications.